Aeolian Research 45 (2020) 100601

Contents lists available at ScienceDirect

Aeolian Research

journal homepage: www.elsevier.com/locate/aeolia

A wind tunnel study of the effect of intermediate density ratio on saltation threshold

Devon M. Burr[a,b,*], Stephen L.F. Sutton[a], Joshua P. Emery[a,b], Emily V. Nield[a,c], Jasper F. Kok[d], James K. Smith[e,f], Nathan T. Bridges[g,1]

[a] Earth and Planetary Science Department, University of Tennessee-Knoxville, 1621 Cumberland Ave, 602 Strong Hall, Knoxville, TN 37996, USA[2]
[b] Astronomy and Planetary Sciences Department, Northern Arizona University, 527 S Beaver St, Flagstaff, AZ 86011-6010, USA[3]
[c] Schulich School of Business, York University, Toronto, ON, M3J 1P3, Canada[3]
[d] Department of Atmospheric and Oceanic Sciences, University of California, Los Angeles, CA 90095, USA
[e] Arizona State University, Tempe, AZ 85287-1404, USA
[f] NASA Ames Research Center, Mountain View, CA, USA
[g] Space Department, Johns Hopkins University Applied Physics Laboratory, Laurel, MD 20723, USA

ARTICLE INFO

Keywords:
Density ratio
Laboratory wind tunnel experiments
Saltation threshold
Planetary processes

ABSTRACT

An expression for saltation threshold – the minimum wind speed required to initially saltate particles – is necessary for modeling aeolian processes on Earth and other bodies. Analysis of a compilation of experimental data led to the conclusion that this threshold is a function of the ratio of the density of the particle to that of the entraining fluid (ρ_p/ρ), and to a curve for the dimensionless threshold parameter, $A(\rho_p/\rho)$. Whereas data of low-density ratio and of high-density ratio conditions show constant A values, the single dataset used to define the transitional region of the curve shows a range of values. To revisit this transitional region, we collect new freestream threshold data at 1–20 bars (1–20 × 10^5 Pa) with particles 150–1000 μm in diameter and having densities 400–3300 kg/m^3 using the Titan Wind Tunnel. From these new data spanning a range of intermediate density ratios, we calculate friction wind speeds and values for $A(\rho_p/\rho)$. We filter our threshold data for the same conditions (particle diameter > 200 μm, particle Reynolds number > 10) as in previous work and combine them with previously published data to derive a new density ratio curve with the same form as the previous expression. This new curve of $A(\rho_p/\rho)$, with different parameter values and including uncertainties, confirms the slope in the transitional region between low- and high-density ratios, though giving slightly higher values for A. This work offers improved prediction of threshold wind speeds under thicker-than-terrestrial atmospheres on other solar or extrasolar planets, while also suggesting current challenges to accurate experimental simulation of aeolian transport under such conditions.

1. Introduction

Evidence for the geophysical processes by which granular solids are entrained into transport across solid surfaces by flowing gas is pervasive across the Solar System. Such aeolian movement of sediment – whether by atmospheric, exospheric, or episodic (geysering, jetting) gas flow – has been documented on Earth, Mars, Venus, Titan, Triton, Enceladus, Pluto, and comets (Greeley and Iversen, 1985 and references therein; Sagan and Chyba, 1990; Weitz et al., 1994; Porco et al., 2006; A'Hearn et al., 2011; Lorenz and Zimbelman, 2014 and references therein; Burr et al., 2015b and references therein; Diniega et al., 2017; Jia et al., 2017; Telfer et al., 2018). These processes differ as a function of different boundary conditions, including the sizes of the grains and the speed of the flowing gas (Bagnold, 1941), the densities of the granular solids and the flowing gas (Greeley et al., 1980; Iversen et al., 1987), the relative humidity of the gas and water content of the grains (McKenna Neuman and Sanderson, 2008; Yu et al., 2017), and other conditions (see, e.g., Rasmussen et al., 2015 and references therein).

One descriptor of aeolian processes is the minimum, or threshold, wind speed needed to entrain sediment. Fluid or static threshold is the

* Corresponding author at: Astronomy and Planetary Sciences Department, Northern Arizona University, 527 S Beaver St, Flagstaff, AZ 86011-6010, USA.
E-mail address: devon.burr@nau.edu (D.M. Burr).
[1] Deceased.
[2] Formerly.
[3] Currently.

https://doi.org/10.1016/j.aeolia.2020.100601
Received 12 August 2019; Received in revised form 19 March 2020; Accepted 1 April 2020

wind speed at which sediment lifting is first initiated solely through fluid force, whereas impact threshold is the lowest wind speed at which sediment transport, once initiated, is sustained through the combination of fluid and impact force (Bagnold, 1941). Values for threshold wind speed and the associated threshold shear stress are fundamental to understanding and modeling all aspects of aeolian transport, including the onset of aeolian sediment movement (Bagnold, 1941), aeolian mass flux (White, 1979; White, 1981), minimum aeolian erosion potential (Sagan et al., 1977) and aeolian erosion effectiveness (Bridges et al., 2005). Thus, they impact our analysis and understanding of phenomena from a local scale, like ventification (Knight, 2008) and dune orientation (Rubin and Hunter, 1987), to the global scale, such as the relative importance of various resurfacing processes (Bridges et al., 2012). Correctly understanding these phenomena provides important information for past climate conditions and climate change (Bridges et al., 1999; Greeley et al., 2000; Golombek et al., 2006; Ewing et al., 2015).

The quantification of threshold wind speeds was laid on a foundation of terrestrial (ambient condition) wind tunnel research (Bagnold, 1941), which continues to advance our understanding through increasingly sophisticated instrumentation and experiments (Holstein-Rathlou et al., 2013; Bennett et al., 2015 and references therein; O'Brien and McKenna Neuman, 2016; Yu et al., 2017). Planetary wind tunnels, which simulate atmospheric density on planetary body surfaces (Merrison et al., 2009; Burr et al., 2015b; Swann and Ewing, 2016; Williams and Smith, 2017, and references therein), have enabled the exploration of the effects on aeolian transport of extraterrestrial boundary conditions. Early planetary wind tunnel work assumed that gravity similitude could be attained by variations in the density of the grains (e.g., Greeley et al., 1974), whereas the subsequent history of research into aeolian entrainment and transport processes indicates the need for careful matching of the similitude parameter according to the aeolian process under examination (Burr et al., 2015a; Burr et al., 2015b). Some degree of modeling based on wind tunnel results is necessary to account for gravitational and other differences (e.g., temperature) that have not been achieved in planetary wind tunnels (although see Marshall et al., 1991 for a study of aeolian attrition and accretion under Venusian temperatures and pressures).

The Planetary Aeolian Laboratory at the NASA Ames Research Center in Mountain View, CA, currently supports wind tunnel simulation of extraterrestrial aeolian processes with air densities similar to those at the surface of Mars in the Mars Surface Wind Tunnel (MARSWIT; Greeley et al., 1976; Greeley et al., 1980; Swann and Ewing, 2016; Williams and Smith, 2017). The facility also enabled simulation of the atmospheric density at the surface of Venus in the Venus Wind Tunnel (VWT; Iversen and White, 1982; Greeley et al., 1984; Marshall and Greeley, 1992). A refurbishment of that equipment led to the Titan Wind Tunnel (TWT; Burr et al., 2015b), which can be used to simulate aspects of the atmosphere, such as density or kinematic viscosity (Burr et al., 2015a), on the surface of Titan.

This simulation provides the means to investigate the effects of atmospheric density, pressure, or kinematic viscosity on threshold wind speeds. Threshold wind speeds vary as a function of grain size (Bagnold, 1941), where larger grains require strong winds to overcome greater mass (weight) and smaller grains require stronger winds to overcome interparticle forces (Greeley and Iversen, 1985). The result is a characteristic U-shaped curve for threshold velocity as a function of grain size with an intermediate grain size having the lowest threshold speed. Previous work in the MARSWIT and VWT yielded threshold curves for Mars and Venus (Greeley and Iversen, 1985). Based on the high-pressure VWT work, a threshold curve was also derived for Titan, but not tested at that time against experimental data under Titan similitude conditions.

A synopsis of planetary wind tunnel studies shows repeated mismatching of model output and experimental results (Burr et al., 2015b). Modeling based on terrestrial threshold wind speeds to derive Martian threshold wind speeds was not consistent with later MARSWIT results (Greeley et al., 1976), and likewise, modeling of threshold for Venus surface conditions was not consistent with results from the VWT. To force consistency of the Venus threshold model with the VWT results, a term was included in the expression for threshold that accounts for the low ratio of grain to atmospheric density on Venus (Iversen et al., 1987). More recent modeling of saltation threshold on Titan could be made consistent with TWT results with the inclusion of this density ratio term (Burr et al., 2015a). This term is based on the assumed influence of grain impacts on the bed, lowering the threshold curve that results from gas (or fluid) flow alone (Iversen et al., 1987). This assumption is reasonable for the higher density ratio conditions on Earth and Mars, under which fluid threshold is higher than impact threshold (Kok et al., 2012), so that when threshold is observed, impacts are necessarily important. However, numerical modeling results indicate that the fluid threshold under both Venus and Titan conditions is lower than the impact threshold (Kok et al., 2012). Thus, for the lower density ratio conditions on Venus and Titan, the physical justification for the density ratio term remains unclear. Numerical simulations by Durán et al. (2012) demonstrate that density ratio "is a true dimensionless parameter of the problem" and suggest that the empirical density ratio term employed by Iversen et al. (1987) encapsulates the physical transition from fluid threshold to impact threshold.

These prior VWT data were collected under a single pressure and so with a limited range of density ratios, resulting from only the variability in the grain densities of ~3x. To investigate further the effect of the density ratio term on threshold and its validity, we collected new data at a larger range of gas densities and thus a larger range of density ratio conditions than in previous recent work. These new data do not include the extrema of density ratio values previously published, in which a compilation of value for water and from terrestrial wind tunnels gave low and high extreme values, respectively (Iversen et al., 1987). Instead, we used the TWT to focus on the transitional region occupied by Venus and Titan conditions. We compared these new data to previously collected data from the VWT and to the VWT portion of the threshold curve. The results of the work presented here confirm the slope of the curve in this region and also yield new parameter values for the curve.

2. Background

2.1. Derivation of expressions for planetary aeolian threshold

Expressions for threshold wind speeds were provided by Bagnold (1941), in which threshold is quantified as a friction speed (u_{*t}), a characteristic velocity that describes the magnitude of shear at the surface. Using a conceptualized force balance at the moment of entrainment, Bagnold derived the threshold friction speed, u_{*t}, as:

$$u_{*t} = A\sqrt{\frac{\rho_p - \rho}{\rho} g D_p} \quad (1)$$

where A is the dimensionless threshold parameter, ρ_p is the particle density, D_p is the mean particle diameter, and g is the gravitational acceleration. As $u = \sqrt{(\tau/\rho)}$, where u is flow speed and τ is shear stress, A is equivalent to the square root of the Shields criterion, $\theta = \tau/[(\rho_p\text{-}\rho)\, g D_p]$, for the initiation of sediment motion in a fluid flow. Bagnold suggested that A is dependent on the particle friction Reynolds number at threshold (Re_{*t}), defined as:

$$Re_{*t} = \frac{u_{*t} D_p}{\nu} \quad (2)$$

where ν is the kinematic viscosity (the ratio of the fluid dynamic viscosity to fluid density). However, by negating this dependence on Re_{*t}, the interparticle force, and the lift force, A was simplified to 0.1 for all grains with a diameter >250 μm, based on terrestrial experimental data (Bagnold, 1941).

Later experiments under ambient (terrestrial) conditions in the Iowa

Table 1
(top) Expressions for A as a function of Reynolds number, with a generic formulation, followed by specific expressions for A. (bottom) Dependence of I_p on D_p. The values from Iversen and White (1982) and Greeley and Iversen (1985) are also shown in the values for n and K in the rows above.

Generic formulation (Iversen et al. 1976a,b):

$$A = C\left(1 + \frac{K}{\rho_p g D_p^n}\right)^{1/2} f(Re_{*t})$$

Reference	Re_{*_t} range	Expression for A
Greeley and Iversen (1985)	$0.03 \le Re_{*_t} \le 3$	$A = 0.2\frac{\left(1 + \frac{0.006}{\rho_p g D_p^{2.5}}\right)^{1/2}}{(1 + 2.5Re_{*t})^{1/2}}$ A $= 0.129\frac{\left(1 + \frac{0.006}{\rho_p g D_p^{2.5}}\right)^{\frac{1}{2}}}{(1.928 Re_{*t}^{0.092} - 1)^{\frac{1}{2}}}$
Iversen and White (1982)	$3 \le Re_{*_t} \le 10$	$A = 0.129\frac{\left(1 + \frac{0.006}{\rho_p g D_p^{2.5}}\right)^{\frac{1}{2}}}{(1.928 Re_{*t}^{0.092} - 1)^{\frac{1}{2}}}$
Iversen and White (1982)	$Re_{*_t} \ge 10$	$A = 0.120\left(1 + \frac{0.006}{\rho_p g D_p^{2.5}}\right)^{\frac{1}{2}}(1 - 0.0858e^{[-0.0617(Re_{*t} - 10)]})$

Reference	Dependence of I_p on D_p	Origin
Iversen et al. (1976b, 1987)	$I_p = [0.055/(\rho_p g D_p^2)\ ]^{1/2}$	Value of n set as 2, so $I_p = I_p\, f(D_p)$; value of K fitted to terrestrial wind tunnel data
Iversen and White (1982), Greeley and Iversen (1985)	$I_p = [0.006/(\rho_p g D_p^{2.5})\ ]^{1/2}$	Values of n and K fitted to MARSWIT data

State University (ISU) Wind Tunnel tested the validity of Bagnold's threshold equation (Eq. (1)) (Iversen et al., 1976a; Iversen et al., 1976b). Results indicated that A is not uniquely a function of Re_{*_t} but also depends on interparticle force (parameterized by the exponent n; see expressions for A, Table 1). This result led to a generic equation that describes the functional behavior of the dimensionless threshold parameter, A, in different flow regimes, where K is a constant having units of g cm^{-2} sec^{-2}. Experiments in the MARSWIT simulating aeolian processes in a low pressure environment yielded data that were inconsistent with the predictions based on mathematical extrapolation from ambient conditions (Greeley et al., 1976). Fitting the mathematical expression to the data with different assumptions led to defining different formulae for A for a given range of Re_{*t} (Table 1). The value of n has varied depending on whether it was set *a priori* to a presumed value or fit to data. A value for n of 2.5 was derived from fitting the MARSWIT experimental data (Table 1).

The literature states that the experiments under these low-fluid-density conditions were considered to involve fluid ("static") threshold only (Greeley et al., 1977, p. 10), in which entrainment is only a function of fluid flow. However, numerical modeling has shown that under low-fluid-density conditions, impact threshold, with the impact force of upwind grains contributing to entrainment, occurs at a significantly lower wind speed than does fluid threshold (Kok, 2010). Threshold in the MARSWIT was defined as "the movement of particles over the entire bed" (Table 2). Such wide-spread movement was unlikely to have occurred simultaneously, as experiments and field data show that initial movement occurs as individual grains or small groups of grains (Bagnold, 1941; Nickling, 1988), and these initial grains would have impacted the downwind bed. Thus, the observation of threshold in the MARSWIT was likely a result of some (unobserved) impact by upwind grains.

Using this refined threshold model derived from wind tunnel data for relatively low-density (Martian and terrestrial) conditions, threshold wind speeds for Venusian conditions as a function of grain size were calculated (Iversen and White, 1982). However, data from the VWT simulating entrainment under high pressure (Venusian) conditions (Greeley et al., 1984) were not consistent with this calculation (Iversen et al., 1987). This inconsistency was ascribed to the effect of grain impact, which had not been accounted for in previous force-balance equations used to derive threshold under the (likely incorrect) presumption of fluid threshold. The model was corrected to the VWT data by introducing into the formula for A a density ratio term, $f(\rho_p/\rho)$, where ρ_p is the density of the particle and ρ is the density of the fluid (Eq. (3)).

2.2. The density ratio term

In previous work, determining formulae for A as a function of the density ratio involved compiling a threshold dataset over a range of density ratio conditions, including terrestrial conditions at ISU (Iversen

Table 2
Definitions of threshold movement used in previous wind tunnel studies, showing significant differences. This work, like the VWT work, investigated conditions in the transitional region of the density ratio curve. Therefore, for our 2016 data published here, we used the stage of motion – "patches" – that approximated the definition of threshold for the VWT work.

Reference	Wind tunnel	Threshold Definition
Bagnold (1941)	Imperial College Wind Tunnel	The point when "the grains could be seen to have gathered sufficient speed to start bouncing off the ground."
Greeley et al. (1974)	Iowa State University	No definition provided
Greeley et al. (1976)	Martian Surface Wind Tunnel	The speed at which "the movement of particles [occurred] over the entire bed, rather than the movement of only a few individual particles."
Greeley et al. (1980)	Martian Surface Wind Tunnel	The speed at which "grains of a given size are set into motion over an entire bed."
Greeley et al. (1984)	Venus Wind Tunnel	"The speed at which groups of grains began to saltate sporadically."
Burr et al. (2015a)	Titan Wind Tunnel	The speed at which "50% of the bed [is] in motion, indicating that one-half of the grains have exceeded threshold and the other half have not."
This work (definition of "patches" from Burr et al., 2015a)	Titan Wind Tunnel	The speed at which "continuous grain motion [is] occurring over less than 50% of the bed."

Table 3
Summary table of the experimental results, including the sediment properties, boundary conditions including density ratio, u_∞ at threshold, and the dimensionless threshold parameter, A. Experiment numbers "T = 16-####" indicate experiments performed during 2016 in sequential (time) order. Empty cells indicate that data could not be observed or values could not be calculated. The table shows data taken at patches (Table 2) with increasing fan motor speed that satisfied both criteria for particle Reynolds number at threshold and grain diameter, and so may be used to derive the density ratio expression. These data are shown plotted in Figs. 9 and 10. All collected data at all stages of motion, both increasing and decrease fan motor speeds, regardless of satisfying the criteria in deriving the density ratio expression, are included in the Supplemental Materials, Table3_for_Supplement.xlsx.

Experimental Parameters														rescaled Freestream Height δ (m) = 0.023						Test	Test	Test	
Material and Size Range	Experiment Number	Desired Pressure (bar)	Calc. air density (kg m^{-3})	Kinematic viscosity (m^2 s^{-1})	Particle Reynolds number	$u_{infinity}$ (m s^{-1})	Std Dev. (m s^{-1})	Grain diam. (m)	Grain density (kg m^{-3})	Density ratio (ρ_p/ρ_f)	(ρ_p -ρ_f) / ρ_f	z_0	$u_{infinity}$ (m s^{-1})	Std Dev. (m s^{-1})	A	Particle Reynolds number, Re^*_p	Grain Diameter, d (microns)	u^*_t (m s^{-1})	Re^*_p >10	d>250	Both	u^*_t for Re^*_p >10 and d >250
Walnut 833-1000 μm	T-16-1294	20	23.52	7.74E-07	117	2.46	0.08	0.0009	1100	47	46	3.1E-05	1.6	0.10	0.15	117	916.50	0.10	TRUE	TRUE	TRUE	0.10
	T-16-1295	15	17.68	1.03E-06	115	3.29	0.08	0.0009	1100	62	61	3.1E-05	2.1	0.13	0.17	115	916.50	0.13	TRUE	TRUE	TRUE	0.13
	T-16-1296	12.5	14.78	1.23E-06	108	3.69	0.12	0.0009	1100	74	73	3.1E-05	2.3	0.14	0.18	108	916.50	0.14	TRUE	TRUE	TRUE	0.14
	T-16-1297	8	9.45	1.93E-06	85	4.62	0.15	0.0009	1100	116	115	3.1E-05	2.9	0.18	0.18	85	916.50	0.18	TRUE	TRUE	TRUE	0.18
	T-16-1298	3	3.52	5.17E-06	51	7.55	0.08	0.0009	1100	312	311	3.1E-05	4.6	0.29	0.17	51	916.50	0.29	TRUE	TRUE	TRUE	0.29
	T-16-1299	3	3.52	5.17E-06	51	7.63	0.07	0.0009	1100	312	311	3.1E-05	4.7	0.29	0.17	51	916.50	0.29	TRUE	TRUE	TRUE	0.29
	T-16-1300	8	9.45	1.93E-06	81	4.40	0.16	0.0009	1100	116	115	3.1E-05	2.8	0.17	0.17	81	916.50	0.17	TRUE	TRUE	TRUE	0.17
	T-16-1301	12.5	14.70	1.24E-06	110	3.81	0.10	0.0009	1100	75	74	3.1E-05	2.4	0.15	0.18	110	916.50	0.15	TRUE	TRUE	TRUE	0.15
	T-16-1302	20	23.47	7.75E-07	128	2.71	0.07	0.0009	1100	47	46	3.1E-05	1.7	0.11	0.17	128	916.50	0.11	TRUE	TRUE	TRUE	0.11
	T-16-1303	20	23.44	7.77E-07	145	3.11	0.05	0.0009	1100	47	46	3.1E-05	2.0	0.12	0.19	145	916.50	0.12	TRUE	TRUE	TRUE	0.12
	T-16-1304	15	17.71	1.03E-06	118	3.35	0.09	0.0009	1100	62	61	3.1E-05	2.1	0.13	0.18	118	916.50	0.13	TRUE	TRUE	TRUE	0.13
	T-16-1305	15	17.63	1.03E-06	120	3.45	0.10	0.0009	1100	62	61	3.1E-05	2.2	0.14	0.18	120	916.50	0.14	TRUE	TRUE	TRUE	0.14
	T-16-1306	12.5	14.66	1.24E-06	103	3.55	0.11	0.0009	1100	75	74	3.1E-05	2.2	0.14	0.17	103	916.50	0.14	TRUE	TRUE	TRUE	0.14
	T-16-1307	8	9.45	1.93E-06	84	4.55	0.15	0.0009	1100	116	115	3.1E-05	2.8	0.18	0.17	84	916.50	0.18	TRUE	TRUE	TRUE	0.18
	T-16-1308	3	3.52	5.17E-06	49	7.26	0.11	0.0009	1100	312	311	3.1E-05	4.5	0.28	0.17	49	916.50	0.28	TRUE	TRUE	TRUE	0.28
Beach 833-1000 μm	T-16-1325	20	23.34	7.80E-07	168	3.66	0.04	0.0009	2500	107	106	3.1E-05	2.3	0.14	0.15	168	916.50	0.14	TRUE	TRUE	TRUE	0.14
	T-16-1326	15	17.70	1.03E-06	164	4.75	0.07	0.0009	2500	141	140	3.1E-05	3.0	0.18	0.16	164	916.50	0.18	TRUE	TRUE	TRUE	0.18
	T-16-1327	12.5	14.77	1.23E-06	147	5.15	0.03	0.0009	2500	169	168	3.1E-05	3.2	0.20	0.16	147	916.50	0.20	TRUE	TRUE	TRUE	0.20
	T-16-1328	8	9.49	1.92E-06	113	6.20	0.00	0.0009	2500	263	262	3.1E-05	3.8	0.24	0.15	113	916.50	0.24	TRUE	TRUE	TRUE	0.24
	T-16-1329	8	9.44	1.93E-06	113	6.22	0.00	0.0009	2500	265	264	3.1E-05	3.8	0.24	0.15	113	916.50	0.24	TRUE	TRUE	TRUE	0.24
	T-16-1330	12.5	14.71	1.24E-06	148	5.17	0.01	0.0009	2500	170	169	3.1E-05	3.2	0.20	0.16	148	916.50	0.20	TRUE	TRUE	TRUE	0.20
	T-16-1331	15	17.62	1.03E-06	165	4.83	0.00	0.0009	2500	142	141	3.1E-05	3.0	0.19	0.17	165	916.50	0.19	TRUE	TRUE	TRUE	0.19
	T-16-1332	20	23.41	7.77E-07	224	4.92	0.14	0.0009	2500	107	106	3.1E-05	3.1	0.19	0.19	224	916.50	0.19	TRUE	TRUE	TRUE	0.19
	T-16-1333	20	23.41	7.77E-07	199	4.36	0.06	0.0009	2500	107	106	3.1E-05	2.7	0.17	0.17	199	916.50	0.17	TRUE	TRUE	TRUE	0.17
	T-16-1334	15	17.65	1.03E-06	165	4.81	0.02	0.0009	2500	142	141	3.1E-05	3.0	0.19	0.17	165	916.50	0.19	TRUE	TRUE	TRUE	0.19
Basalt 500-707 μm	T-16-1344	12.5	14.70	1.24E-06	64	3.58	0.09	0.0006	3300	224	223	2E-05	2.3	0.13	0.11	64	603.50	0.13	TRUE	TRUE	TRUE	0.13
	T-16-1345	8	9.47	1.92E-06	53	4.67	0.09	0.0006	3300	348	347	2E-05	2.9	0.17	0.12	53	603.50	0.17	TRUE	TRUE	TRUE	0.17
	T-16-1347	8	9.39	1.94E-06	52	4.59	0.11	0.0006	3300	351	350	2E-05	2.9	0.17	0.12	52	603.50	0.17	TRUE	TRUE	TRUE	0.17
	T-16-1348	8	9.41	1.93E-06	59	5.27	0.12	0.0006	3300	351	350	2E-05	3.3	0.19	0.13	59	603.50	0.19	TRUE	TRUE	TRUE	0.19
	T-16-1349	12.5	14.70	1.24E-06	69	3.83	0.22	0.0006	3300	224	223	2E-05	2.4	0.14	0.12	69	603.50	0.14	TRUE	TRUE	TRUE	0.14
	T-16-1350	12.5	14.68	1.24E-06	79	4.45	0.10	0.0006	3300	225	224	2E-05	2.8	0.16	0.14	79	603.50	0.16	TRUE	TRUE	TRUE	0.16
Charcoal 250-300 μm	T-16-1351	20	23.38	7.79E-07	12	0.91	0.34	0.0003	400	17	16	9.2E-06	0.7	0.04	0.17	12	275.00	0.04	TRUE	TRUE	TRUE	0.04
	T-16-1352	15	17.62	1.03E-06	12	1.25	0.06	0.0003	400	23	22	9.2E-06	0.9	0.05	0.19	12	275.00	0.05	TRUE	TRUE	TRUE	0.05
	T-16-1353	12.5	14.74	1.23E-06	11	1.32	0.08	0.0003	400	27	26	9.2E-06	0.9	0.05	0.18	11	275.00	0.05	TRUE	TRUE	TRUE	0.05
	T-16-1360	12.5	14.65	1.24E-06	11	1.38	0.07	0.0003	400	27	26	9.2E-06	1.0	0.05	0.19	11	275.00	0.05	TRUE	TRUE	TRUE	0.05
	T-16-1361	15	17.55	1.04E-06	13	1.34	0.07	0.0003	400	23	22	9.2E-06	0.9	0.05	0.20	13	275.00	0.05	TRUE	TRUE	TRUE	0.05
	T-16-1362	20	23.34	7.80E-07	16	1.23	0.09	0.0003	400	17	16	9.2E-06	0.9	0.05	0.22	16	275.00	0.05	TRUE	TRUE	TRUE	0.05
	T-16-1363	20	23.42	7.77E-07	15	1.18	0.10	0.0003	400	17	16	9.2E-06	0.8	0.04	0.21	15	275.00	0.04	TRUE	TRUE	TRUE	0.04
	T-16-1365	12.5	14.78	1.23E-06	12	1.44	0.06	0.0003	400	27	26	9.2E-06	1.0	0.05	0.20	12	275.00	0.05	TRUE	TRUE	TRUE	0.05
Charcoal 425-500 μm	T-16-1369	20	23.40	7.78E-07	24	0.97	0.19	0.0005	400	17	16	1.5E-05	0.7	0.04	0.15	24	462.50	0.04	TRUE	TRUE	TRUE	0.04
	T-16-1370	15	17.71	1.03E-06	25	1.44	0.09	0.0005	400	23	22	1.5E-05	1.0	0.06	0.18	25	462.50	0.06	TRUE	TRUE	TRUE	0.06
	T-16-1371	12.5	14.83	1.23E-06	25	1.73	0.07	0.0005	400	27	26	1.5E-05	1.2	0.07	0.19	25	462.50	0.07	TRUE	TRUE	TRUE	0.07
	T-16-1372	8	9.54	1.91E-06	18	2.01	0.06	0.0005	400	42	41	1.5E-05	1.3	0.07	0.17	18	462.50	0.07	TRUE	TRUE	TRUE	0.07
	T-16-1377	8	9.41	1.93E-06	18	2.05	0.08	0.0005	400	43	42	1.5E-05	1.4	0.08	0.18	18	462.50	0.08	TRUE	TRUE	TRUE	0.08
	T-16-1378	12.5	14.65	1.24E-06	25	1.82	0.08	0.0005	400	27	26	1.5E-05	1.2	0.07	0.20	25	462.50	0.07	TRUE	TRUE	TRUE	0.07
	T-16-1379	15	17.58	1.04E-06	29	1.74	0.07	0.0005	400	23	22	1.5E-05	1.2	0.07	0.21	29	462.50	0.07	TRUE	TRUE	TRUE	0.07
	T-16-1380	20	23.34	7.80E-07	37	1.64	0.05	0.0005	400	17	16	1.5E-05	1.1	0.06	0.23	37	462.50	0.06	TRUE	TRUE	TRUE	0.06
	T-16-1381	20	23.46	7.76E-07	37	1.62	0.08	0.0005	400	17	16	1.5E-05	1.1	0.06	0.23	37	462.50	0.06	TRUE	TRUE	TRUE	0.06
	T-16-1382	15	17.78	1.02E-06	29	1.72	0.07	0.0005	400	22	21	1.5E-05	1.2	0.06	0.21	29	462.50	0.06	TRUE	TRUE	TRUE	0.06
	T-16-1383	12.5	14.85	1.23E-06	27	1.89	0.09	0.0005	400	27	26	1.5E-05	1.3	0.07	0.21	27	462.50	0.07	TRUE	TRUE	TRUE	0.07
	T-16-1384	8	9.57	1.90E-06	18	2.02	0.21	0.0005	400	42	41	1.5E-05	1.3	0.07	0.17	18	462.50	0.07	TRUE	TRUE	TRUE	0.07
	T-16-1385	3	3.57	5.10E-06	11	3.24	0.06	0.0005	400	112	111	1.5E-05	2.1	0.12	0.16	11	462.50	0.12	TRUE	TRUE	TRUE	0.12
Charcoal 600-707 μm	T-16-1387	20	23.30	7.81E-07	48	1.42	0.05	0.0007	400	17	16	2.2E-05	1.0	0.06	0.18	48	653.50	0.06	TRUE	TRUE	TRUE	0.06
	T-16-1388	15	17.71	1.03E-06	45	1.80	0.06	0.0007	400	23	22	2.2E-05	1.2	0.07	0.19	45	653.50	0.07	TRUE	TRUE	TRUE	0.07
	T-16-1389	12.5	14.80	1.23E-06	43	2.06	0.08	0.0007	400	27	26	2.2E-05	1.4	0.08	0.20	43	653.50	0.08	TRUE	TRUE	TRUE	0.08
	T-16-1390	8	9.51	1.91E-06	33	2.56	0.09	0.0007	400	42	41	2.2E-05	1.7	0.10	0.19	33	653.50	0.10	TRUE	TRUE	TRUE	0.10
	T-16-1391	3	3.53	5.16E-06	16	3.45	0.07	0.0007	400	113	112	2.2E-05	2.2	0.13	0.15	16	653.50	0.13	TRUE	TRUE	TRUE	0.13
	T-16-1394	3	3.52	5.17E-06	15	3.14	0.06	0.0007	400	114	113	2.2E-05	2.0	0.12	0.14	15	653.50	0.12	TRUE	TRUE	TRUE	0.12
	T-16-1395	8	9.39	1.94E-06	32	2.45	0.06	0.0007	400	43	42	2.2E-05	1.6	0.09	0.18	32	653.50	0.09	TRUE	TRUE	TRUE	0.09
	T-16-1396	12.5	14.69	1.24E-06	43	2.10	0.08	0.0007	400	27	26	2.2E-05	1.4	0.08	0.20	43	653.50	0.08	TRUE	TRUE	TRUE	0.08
	T-16-1397	15	17.61	1.03E-06	50	2.02	0.08	0.0007	400	23	22	2.2E-05	1.3	0.08	0.21	50	653.50	0.08	TRUE	TRUE	TRUE	0.08
	T-16-1398	20	23.40	7.78E-07	66	2.00	0.06	0.0007	400	17	16	2.2E-05	1.3	0.08	0.24	66	653.50	0.08	TRUE	TRUE	TRUE	0.08
	T-16-1399	20	23.49	7.75E-07	62	1.86	0.05	0.0007	400	17	16	2.2E-05	1.2	0.07	0.23	62	653.50	0.07	TRUE	TRUE	TRUE	0.07
	T-16-1400	15	17.74	1.03E-06	51	2.04	0.08	0.0007	400	23	22	2.2E-05	1.3	0.08	0.21	51	653.50	0.08	TRUE	TRUE	TRUE	0.08
	T-16-1401	12.5	14.84	1.23E-06	48	2.33	0.10	0.0007	400	27	26	2.2E-05	1.5	0.09	0.22	48	653.50	0.09	TRUE	TRUE	TRUE	0.09
	T-16-1402	8	9.53	1.91E-06	36	2.77	0.12	0.0007	400	42	41	2.2E-05	1.8	0.10	0.20	36	653.50	0.10	TRUE	TRUE	TRUE	0.10
	T-16-1403	3	3.57	5.10E-06	18	3.68	0.07	0.0007	400	112	111	2.2E-05	2.3	0.14	0.16	18	653.50	0.14	TRUE	TRUE	TRUE	0.14

et al., 1976b), under low pressure conditions at MARSWIT (Greeley et al., 1980), under high pressure conditions at the VWT (Greeley et al., 1984) and with water as the fluid (Graf, 1971). These threshold data were then filtered so that (1) the grain diameter was >200 μm, eliminating dependence on interparticle forces (see Iversen et al., 1976b, Fig. 2a), and (2) Re_{*_t} was >10, above which *A* becomes independent of the friction threshold Reynolds number (see Iversen et al., 1987, Fig. 2). [We also considered the condition that the roughness Reynolds number at threshold, $Re_{*_r} = \frac{u_{*t} z_0}{\nu}$, be >2.5, suggested as a criterion for accurately simulating a naturally occurring boundary layer (Sutton, 1949, as cited by White, 1996). However, the physical justification for this criterion was not clear to us. We include data filtered for this roughness Reynolds number criterion in Supplemental Materials, Table3_for_Supplement.xlsx (columns CV and CW and last tab) for completeness, but do not apply this filter elsewhere in this work].

The filtered data for *A* were plotted versus the density ratio, ρ_p/ρ, and fitted with a curve (Fig. 1), for which *A* is a function of interparticle forces, Reynolds friction number, Re_{*_t} and the density ratio function, $f(\rho_p/\rho)$. The derivation of the form of the curve in Iversen et al. (1987)

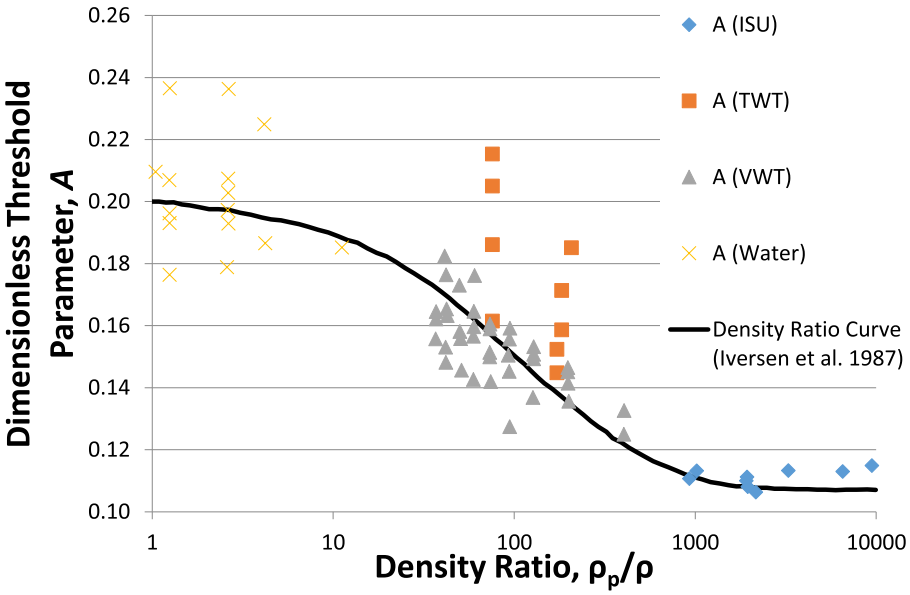

Fig. 1. Threshold parameter A plotted as a function of the density ratio, ρ_p/ρ, where ρ_p is the density of the particle and ρ is the density of the fluid for various fluids. The data are shown for particles > 200 μm diameter and $Re_{*t} > 10$, adapted from Iversen et al. (1987) with their density ratio curve overlain on the data. [Refitting a curve to the Iversen et al. (1987) data indicates that the first exponential parameter is incorrectly rendered as 0.0054 instead of 0.0078]. The legend indicates the facility or medium for the data: ISU is the Iowa State University Wind Tunnel, VWT is the Venus Wind Tunnel, and Water denotes experiments performed in water. A subset of data for the same filtering conditions collected from the Titan Wind Tunnel (Burr et al., 2015a) is also plotted and shown not to fit the curve in this transitional region, providing impetus for this new TWT work. See Supplement Materials Fig. 1_for-Supplemental.xlsx for the data used to make this plot.

omits some steps and contains a typo in first exponential parameter; a full derivation is provided by Nield (2018). The result of the derivation is the expression

$$A^2 = \frac{K}{h(Re_{*t}) + f(\rho_p/\rho)} \tag{3}$$

consistent with the generic form shown in Table 1. The shape of the curve (Fig. 1) shows that the expression for A is sigmoidal and thus has the form $1/(1 + e^{-x})$, which can be rewritten as:

$$A = \alpha / \sqrt{1 + \beta\left(1 - e^{\left(-\gamma\left(\frac{\rho_p}{\rho} - 1\right)^{\lambda}\right)}\right)} \tag{4}$$

where α, β, γ, and λ are constants.

The numerator, α, represents the upper limit of the sigmoidal

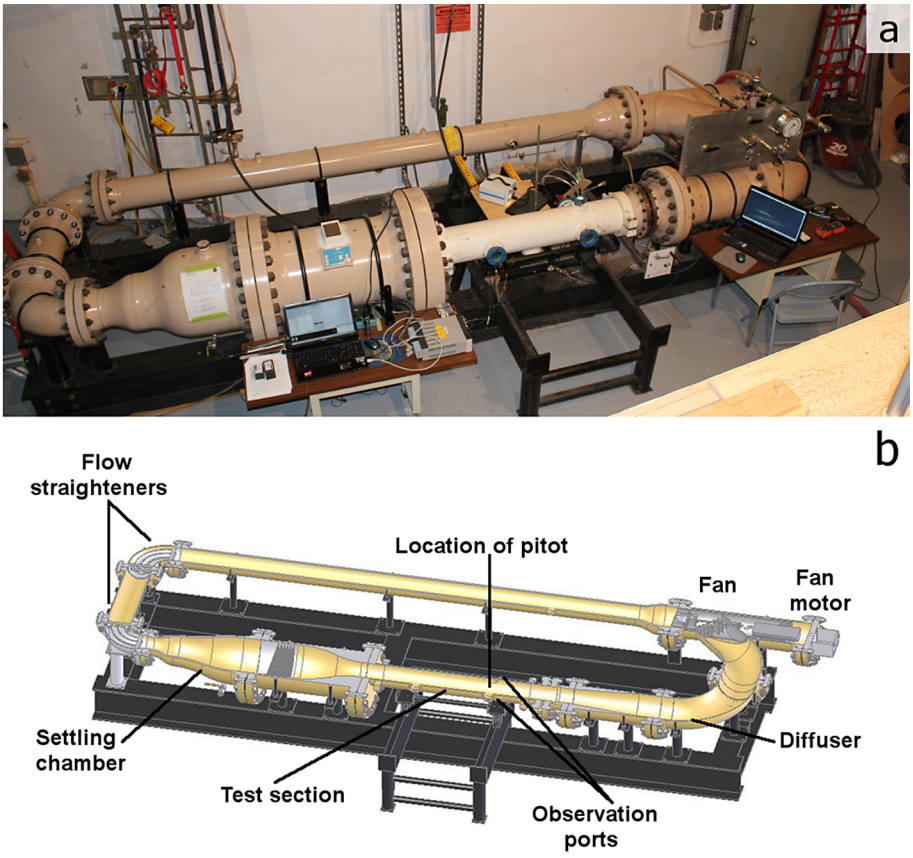

Fig. 2. (a) Photograph of the Titan Wind Tunnel. (b) Sectioned layout of the Titan Wind Tunnel. For clarity, only the downwind observational ports are labeled; the upwind port is visible in the photograph. Modified from Burr et al. (2015b).

function for A, i.e., when the density ratio term, $f(\rho_p/\rho)$, approaches 1. Its value of 0.2 was derived by Iversen et al. (1987) using experimental measurements (Chepil, 1958; Coleman, 1967). The lower limit of 0.11 was derived under terrestrial conditions (Bagnold, 1941; Iversen et al., 1976b). Substituting in these coefficients for the upper and lower limits of the sigmoidal function yields

$$A = 0.2/\sqrt{1 + 2.3(1 - e^{-0.0078(\rho_p/\rho - 1)^{0.86}})} \quad (5)$$

(see Nield, 2018, for a full derivation).

Although its derivation was impelled by data under intermediate density ratio (i.e., Venus Wind Tunnel) conditions, this continuous expression was intended to correct the previous formulations so as to align with experimental results at all density ratio conditions. At density ratios > 1000, as for atmospheric conditions on Earth or Mars, the density ratio term ($f(\rho_p/\rho) = \mathrm{EXP}(-0.0078((\rho_p/\rho) - 1)^{0.86})$) goes to zero and the value for A of 0.11 as derived by Bagnold (1941) for terrestrial conditions is recovered. At intermediate density ratios, as on Venus (or Titan), this term increases and the expression for A correspondingly increases. As the density ratio approaches 1, as experienced in fluvial environments on Earth, the value of A approaches the limiting value of 0.2.

2.3. Methodology: Testing the expression for A

The TWT (Fig. 2) (Burr et al., 2015b) provides an opportunity to quantify threshold wind speeds under Titan analogue conditions. Those data, like the data from the VWT, fall in the intermediate density ratio space that is transitional between fluvial (water) and aeolian conditions on Earth. Our methodology (Fig. 3) was to collect freestream TWT data at threshold conditions for different density ratios, reduce them to friction wind speeds, filter them to eliminate the effects of particle friction Reynolds number and interparticle forces following Iversen et al (1987), and compare the results to the published density ratio curve. As a pressure vessel, the TWT is limited in size, providing limited access to the test section interior, and instrumentation to collect sediment flux was not in place for these experiments.

2.4. Threshold data collection using the Titan wind tunnel

The similitude boundary condition used for these threshold experiments was kinematic viscosity (Burr et al. 2015a). This choice contrasts with that of VWT work, for which the similitude parameter was density, but was made to provide the correct ratio of lift and drag forces and to simulate the viscous sublayer thicknesses. The surface atmospheric pressure on Titan is ~1.4 bar (1.4×10^5 Pa), but, given the difference in temperature between the surface of Titan and the Titan Wind Tunnel, higher pressures were necessary in order to recreate the kinematic viscosity conditions of Titan's atmosphere in the wind tunnel for current (Burr et al., 2015a, Extended Data Table 1) and past climates. For these density ratio experiments, the TWT pressure varied from 1 to 20 bars (1 to 20×10^5 Pa) in order to achieve a greater range of density ratio conditions. Data evaluation and filtering are explained under Results.

The experimental materials cover a range of partile diameters (250–1000 μm) and particle densities (400 – 3300 kg/m^3), which, with the range of air densities, provided data that span the transitional portion of the threshold curve and overlap the parameter space for the density ratio from previous experiments. For all data collection experiments, the experimental sediments were placed in the test section where they were smoothed into a bed of a constant thickness (1 cm). After the bed was laid down, a ruler was placed so as to be viewable through the downwind observation port and briefly videographed for scale. The ruler was removed, and the tunnel was sealed and pressurized. The bed was then pre-conditioned by increasing the fan speed until ~50% of the bed surface was briefly observed to be in motion, in order to provide a more natural texture to the bed and remove any perched grains.

The experimental threshold data were collected in August 2016. Following the procedure developed in previous work, the fan motor speed was incrementally increased through multiple stages of motion (Burr et al., 2015a, Extended Data Supplemental Materials,

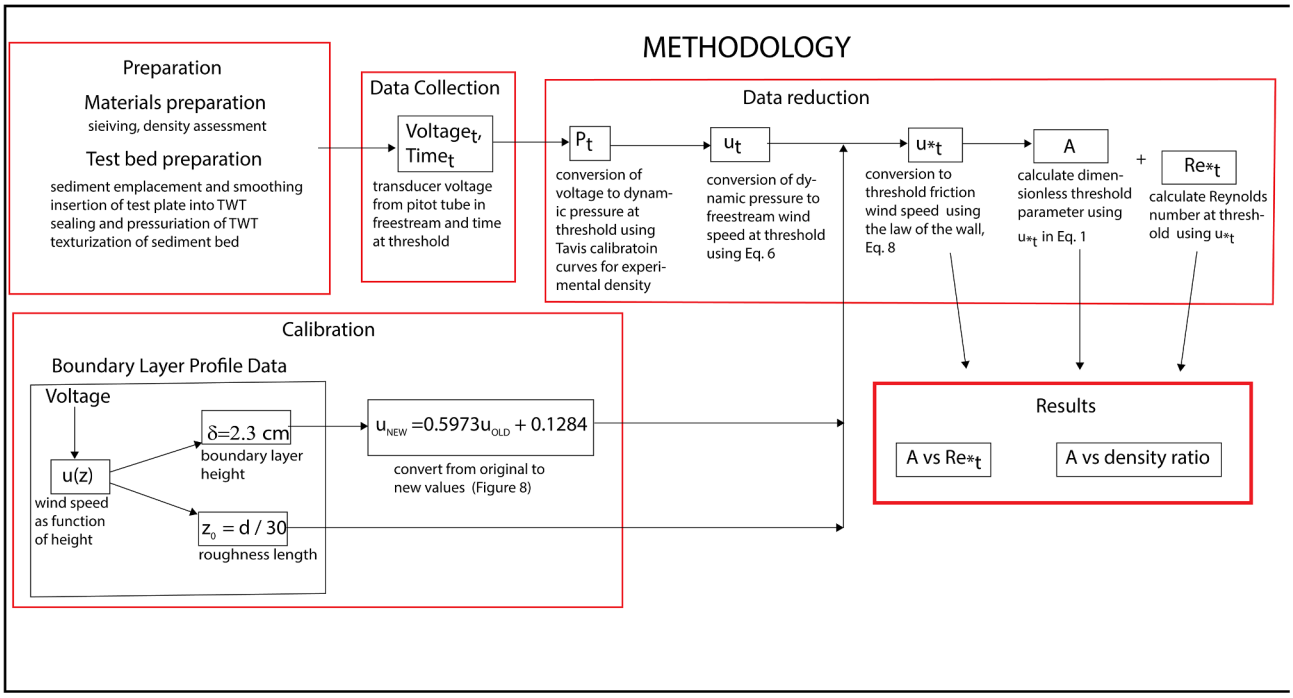

Fig. 3. A flow chart outlining the generic methods used to collect and reduce the data. Under "Calibration," the derivation of u_{OLD} was accomplished with this same methodology but using δ (boundary layer heights) and z_0 (roughness heights) derived from individual boundary layer profiles, before the discovery of the effects of incorrect Pitot configuration (see text for details).

Table3_for_Supplement.xlsx) as perceived by the observer, who recorded the time of occurrence of each observed stage. Not all stages of motion were perceived in all experiments, particularly for fine-grained sediments. The definition of threshold for the VWT data is "the speed at which groups of grains began to saltate sporadically" (Greeley et al., 1984). Of the TWT stages of motion (Burr et al., 2015a), this VWT definition of threshold matches most closely with the stage of "patches", defined as the speed at which "continuous grain motion [is] occurring . . over less than 50% of the bed. Thus, for comparison between the VWT and TWT data, we used "patches" in this work as the stage of motion to define threshold (Table 2). Three different researchers (DMB, NTB, EVN) served as observers, and no observer bias was detectable in selected analysis of the data. For comparison to data collected during increasing fan motor speeds, data were also collected during decreasing fan motor speeds and are provided in Supplemental Online Material as Table3_for-Supplemental.xlsx, although not used in this work.

During each experiment, a high-pressure transducer measured the differential pressure between a static Pitot tube that sensed the ambient pressure in the wind tunnel and a stagnation Pitot tube that sensed the total pressure, that is, the sum of the ambient pressure and the dynamic pressure due to the air flow. The measure of this differential pressure was continuously output and recorded as voltage while the observer recorded the time for each observed stage of motion.

Videography of different stages of motion was collected with an Edgertronic SC1 high speed video camera positioned outside the tunnel at the downwind side observation portal of the tunnel (Fig. 4). The camera frame rate was set to 500 frames per minute (approximately 8 frames per second) with a field of view of 3.6 cm by 2 cm (1280 pixels by 720 pixels). The camera was focused on the bed under the Pitot tube in the center of the tunnel, which was illuminated by two snake lights. Examples of these videos showing different stages of motion are provided in the Supplemental Online Material.

2.5. Data reduction

Data reduction entailed first matching the times recorded by the observer for threshold to the corresponding voltage data from the transducer. These voltages were then converted into dynamic pressures using manufacturer calibration curves for a range of pressures. The

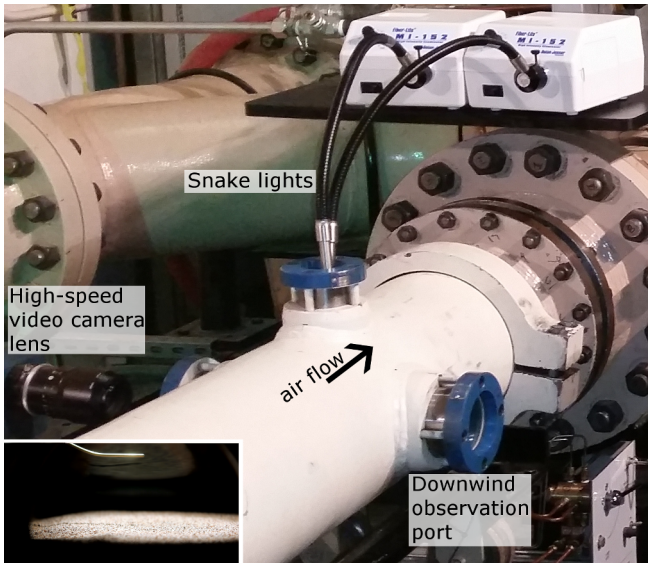

Fig. 4. Experimental setup with the snake lights (rotated from their position in Fig. 1) used to illuminate the grains at the downwind observation port and position of high-speed video camera (showing zoom lens). Inset (lower left) shows view inside of the tunnel as seen by the camera.

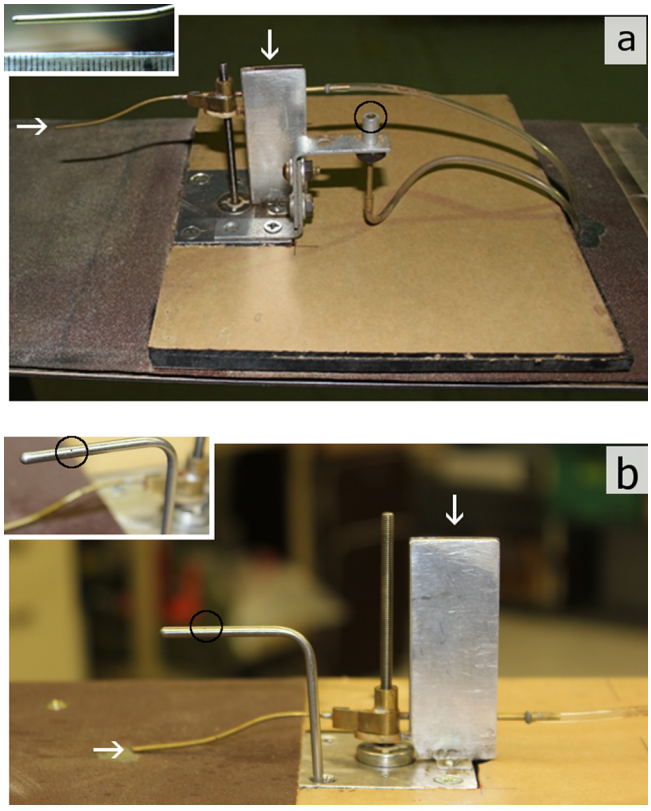

Fig. 5. Images showing old and new Pitot tube configurations. (a) Old: Configuration of the stagnation and static Pitot tubes during initial collection of BLP data. The flat top of the static port (black circle) and its position downwind of the stagnation port stanchion (vertical white arrow) are suspected of causing speed-up over the static port, producing the region of anomalously fast flow observed in the BLPs. Inset (upper left) shows the Pitot tube in the TWT with millimeter-tick marks for scale. (b) New: Configuration of the Pitot tubes during collection of new BLP data to correct the old BLPs, with the static port (black circles in main image and upper left inset) located upwind of the stanchion (vertical white arrow). In both configurations, the traversing Pitot (horizontal white arrows) is used for BLP data collection and is stationary within the freestream for experimental data collection.

resultant dynamic pressures, in turn, were converted to wind speeds at threshold, u, by

$$u = \left(2\frac{P_{dyn}}{\rho}\right)^{1/2}, \tag{6}$$

where P_{dyn} is the dynamic pressure of the gas (air).

Determination of boundary layer profiles in this tunnel is complicated by the pressurization cycling of the tunnel as a whole. During pressurization and venting, significant volumes of air are forced through the Pitot tube ports to maintain pressure equalization. Partial or full blockage of one of the Pitot ports can lead to catastrophically high differential pressures developing in the pressure transducer, resulting in serious damage to the unit (as we have demonstrated). To reduce this risk, the Pitot tube is now operated near the surface of the test plate only with no loose sediments in the tunnel (Fig. 5). In the presence of loose sediments, the wind speed is measured only at the top of the Pitot traverse, 47 mm above the test plate and well above the boundary layer in this tunnel (Fig. 6), providing a good measurement of the freestream velocity, u_∞. This operational restriction necessitates collecting wind profile and u_* data for solving the Law of the Wall without sediment motion and applying those data to conditions with sediment motion.

The law of the wall (also known as the Prandtl-von Kármán equation) gives the relationship of freestream to friction wind speed as a

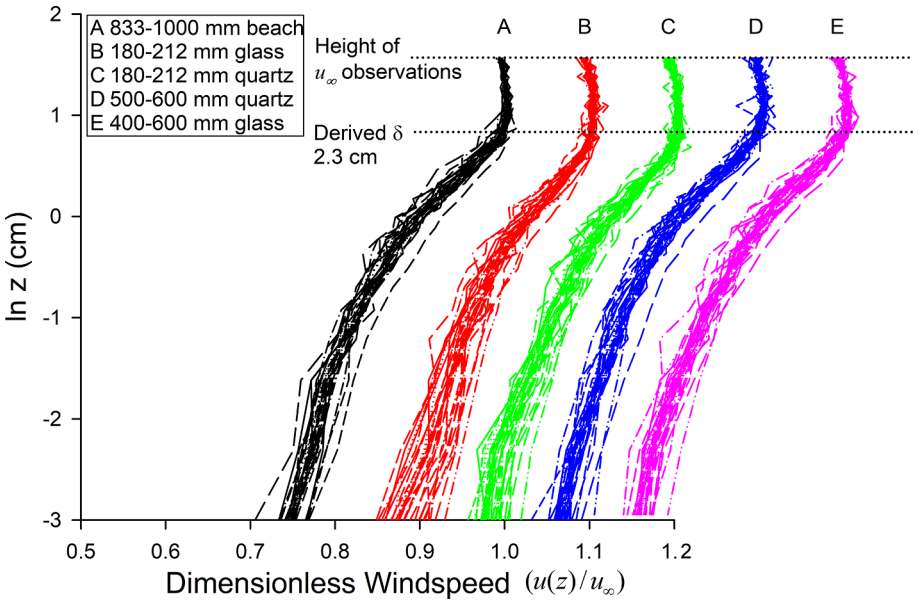

Fig. 6. Plot showing BLPs over several sediments, at tunnel pressures of 8, 12.5, 15 and 20 bar (8, 12.5, 15 and 20 × 10^5 Pa), and fan motor speeds of 20, 25, 40, 50, 60, 75, and 100% capacity. Velocities were normalized by freestream velocity ($u(z)/u_\infty$), and are offset horizontally in increments of 0.1 for clarity. Boundary layer/freestream transition shows high uniformity between and within each sediment grouping, yielding a constant boundary layer height of $\delta = 2.3$ cm. [Note: These BLPs taken with the old configuration (Fig. 5a) were not used to derive roughness height.]

function of the vertical distribution of freestream wind speeds, namely:

$$u_\infty = \frac{u_*}{\kappa} ln \frac{\delta}{z_0} \tag{7}$$

where u_∞ is freestream velocity, δ is the boundary layer thickness, κ is the von Kármán constant (0.41), and z_0 is the aerodynamic roughness height (Bagnold, 1941). This relationship assumes that above the boundary layer height, u_∞ is constant, which is supported by boundary layer data (see Fig. 6). Rearranging the equation to solve for the friction wind speed yields:

$$u_* = \frac{u_\infty \kappa}{ln \frac{\delta}{z_0}}, \tag{8}$$

Thus, in addition to the freestream wind speed, the boundary layer height, δ, and the roughness height, z_0, were required. The boundary layers heights were derived from boundary layer profiles (BLPs) and the roughness heights were approximated as the Nikuradse roughness (Nikuradse, 1933) from the rule of $z_0 = D_p/30$ (White, 2006). This approximation, for conditions of $Re_t > 60$, was supported by analysis of repeated BLP data. However, the BLPs were not taken with sediment movement (due to our concern over clogging of the Pitot), which would sap momentum from the flow, increasing the roughness height. Thus, BLPs without sediment movement yield minimum values as roughness heights for the experimental conditions with sediment movement, but with rough beds (Bauer et al., 2004). Because of this error introduced by the difference in conditions between those of the BLPs and those of the experiments, the approximation of $z_0 = D_p/30$ in Eq. (8) would yield minimum values for the threshold friction wind speed.

Collecting BLPs in July 2016 to derive the boundary layer thickness entailed the construction of fixed roughness beds by gluing sieved sediment onto cardstock paper. To encompass and sample the relevant experimental grain sizes while maintaining operational efficiency, five sediments were used – 180–212 μm glass beads, 180–212 μm quartz sand, 400–600 μm glass beads, 500–600 μm quartz sand, and 833–1000 μm quartzofeldspathic sand. These fixed-sediment beds were placed in the wind tunnel, the tunnel was pressurized, and the fan speed was held constant while a stepping motor moved the Pitot tube through a sequence of positions within the boundary layer. The Pitot tube traversed 25 positions, logarithmically spaced, from 1 mm to 48 mm above the fixed bed. Each position was held for 10 seconds while the transducer attached to the Pitot tube collected voltages. At the end of each traverse, the Pitot was returned in the bed, the fan speed was increased by ~10% or 25%, and another boundary layer profile was collected. The procedure was repeated for a variety of fan motor speeds and atmospheric pressures for each of the three beds.

The voltages from the transducer were averaged for each of the 25 Pitot tube positions and, as for the experimental threshold data, converted to dynamic pressures using manufacturer calibration curves. These dynamic pressures were converted to freestream wind speeds according to Eq. (6). The resultant plot of these wind speeds at each Pitot height yielded the boundary layer profile. Boundary layer thicknesses were designated on these profiles as the locations at which the curves became vertical (Fig. 6). For all five BLPs, the boundary layer height was 2.3 cm, without any detectable trend in value. Consequently, we used $\delta = 2.3$ cm for reducing all experimental data.

2.6. Data correction for Pitot configuration effects

In reducing our 2016 BLPs, we discovered that on plots of u vs ln(z), the data exhibited two straight-line segments below the boundary layer, instead of a single continuous linear segment as expected (Fig. 7). Investigation suggested that this anomalous behavior was a result of the original (2016) Pitot tube configuration (Fig. 5a), in which the static port was located downstream of the Pitot stanchion and oriented vertically, so as to produce a speed-up of air flow. Following some research, we developed a new Pitot tube configuration for which the static pressure is measured via a small hole on the side of a tube located approximately at the same streamwise location as the stagnation Pitot (Fig. 5b). BLP data collected in 2018 with this new configuration show expected behavior without the previously observed segmentation and yield consistent boundary layer heights. We used the 2018 BLP data exclusively in our data reduction.

The experimental data from 2016 were taken with the original (2016) Pitot configuration and thus required correction for this inferred speed-up effect. We reduced the BLP data collected with both the original and new configurations, deriving u_∞ for both configurations. The correspondence of these BLP u_∞ values shows a strong linear relationship (Fig. 8). The equation for this correspondence is

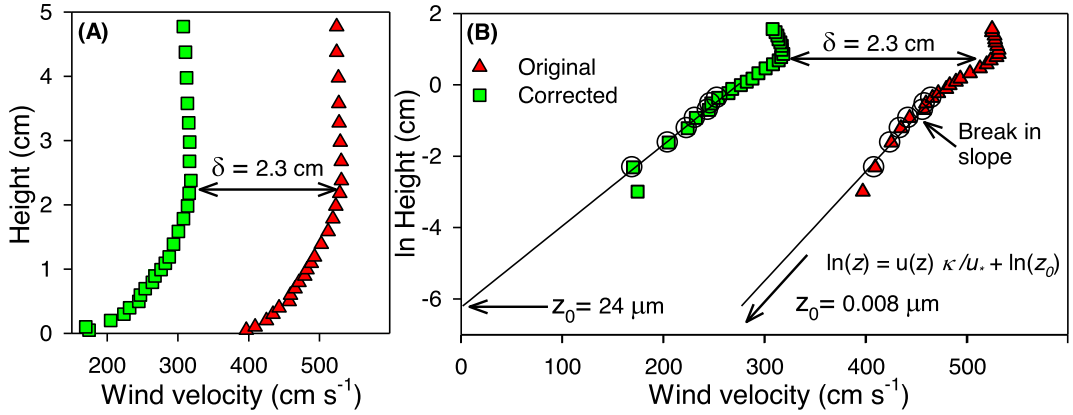

Fig. 7. Boundary layer velocity profiles collected with original Pitot configuration, and with corrected static port. Test bed is 400–600 μm glass beads, tunnel pressure 15 bar (15×10^5 Pa), and 60% fan motor speed. Fig. 7A shows the logarithmic near surface velocity profiles. Fig. 7B shows the same data replotted with a logarithmic velocity axis. The original boundary layer profile (triangles) shows a discontinuity (break) in the slope of the profile and a z_0 value of 8 μm, orders of magnitude smaller than expected (e.g., Nikuradse, 1933). Correction of the Pitot tube configuration (Fig. 5) corrected both issues, and also reduced the derived velocities. See Supplement Materials Fig. 7_for-Supplemental.xlsx for the data used to make this plot.

$u_{\infty NEW} = 0.5973 u_{\infty OLD} + 0.1284$ ($R^2 = 0.9946$). On the basis of this correspondence between the BLP u_∞ values derived with the original Pitot configuration and with the new Pitot configuration, we arithmetically adjusted the original experimental u_∞ values to corrected values.

2.7. Uncertainty analysis

Uncertainty estimates were derived through a similar order of steps as described in previous Titan Wind Tunnel work (Burr et al., 2015a). As the same transducer was used in this as the previous work, the uncertainty in the voltage recorded at the time of threshold, a function of both transducer uncertainty and voltage variability, was taken to be the same value of 2.7%. The uncertainty in conversion from voltage to pressure using the manufacturer-supplied calibration curves is negligible. The uncertainty in previous work of converting pressures measured at a fixed Pitot tube on the opposite side of the wind tunnel from the test section to pressures in the test section was no longer relevant, as the updated configuration allowed for collecting data in the test section itself. The observational uncertainty in the freestream wind speed was

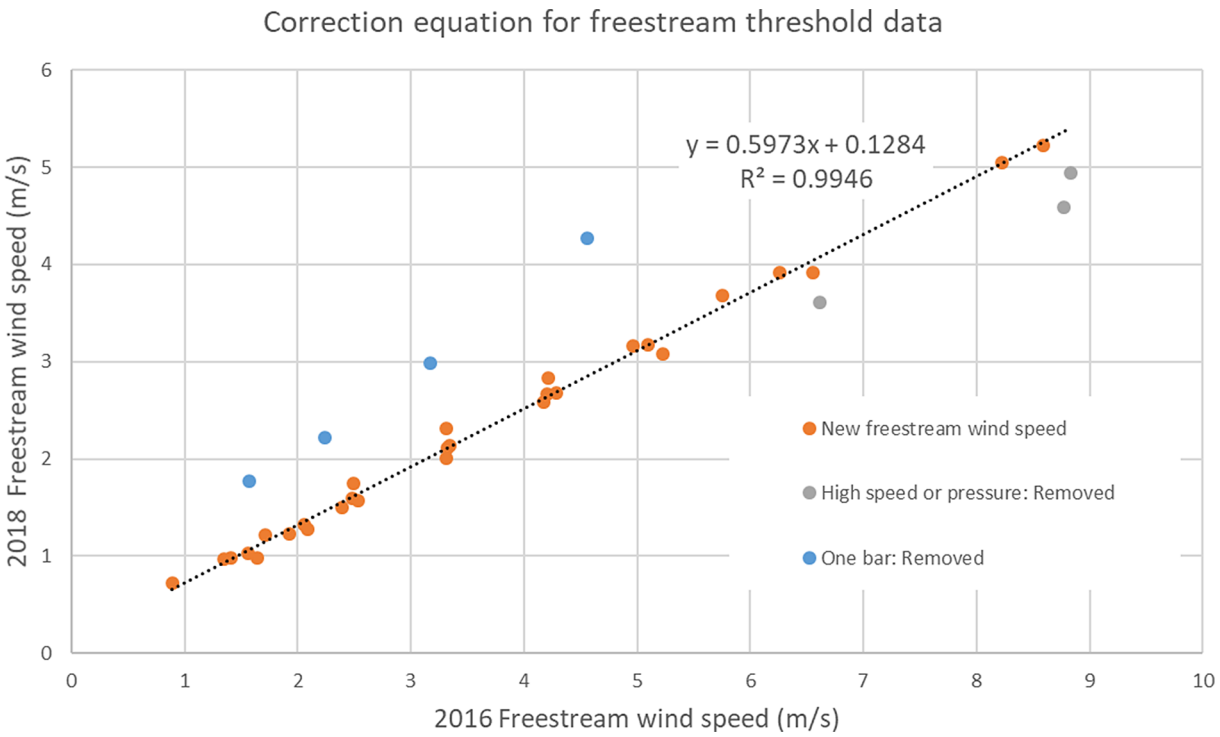

Fig. 8. Data used to derive correlation to convert original freestream wind speeds to corrected values. The data were collected in 2016 with the old configuration (Fig. 5a) and 2018 with the new configuration (Fig. 5b) over 180–212 μm quartz sand, and at 1, 3, 8, 12.5 and 15 bar (1, 3, 8, 12,5, and 15×10^5 Pa). Poor correlation of all data collected at 1 bar, as well as the data collected at the highest velocities and pressures (100% FMS at 12.5 bar, and 75% and 100% at 15 bar), suggest flow effects, and were excluded from our correlation, yielding a strong linear relationship. The equation on the plot was applied to the experimental friction wind speed values (as shown on Fig. 3 in the box labeled Calibration) to correct for enhanced flow over the vertical stagnation port (Fig. 5a). See Supplement Materials Fig. 8_for_Supplemental.xlsx for the data used to make this plot.

derived as the standard derivation of the measurements, provided in the Supplement Materials Table Table3_for-Supplemental.xlsx. We used a single value for the boundary layer height in the law of the wall to convert freestream to friction wind speed (Eq. (8)).

Our use of a single value for the roughness height ($z_0 = D_p/30$; Nikuradse, 1933) links numeric uncertainties in that parameter to the unknown distribution of particle sizes within in the sieve size bins. However, arithmetic inspection shows that the result of uncertainty in the natural logarithm expression has minimal influence on the derived friction threshold values.

3. Results

Out of 193 experiments (summarized in Table3_for-Supplemental.xlsx), we obtained a total of 174 values for u_{*t}. In the remaining 19 experiments, 'patches' – the stage of motion used as threshold in this work – was not observed. Of these 174 experiments, 65 meet both conditions set by Iversen et al. (1987) for deriving the density ratio curve, namely, $Re_{*t} > 10$ and $D_p > 200\,\mu m$ (summarized in Table 3; the smaller number of results provided in Nield, 2018, is superseded by the present work).These new u_{*t}. data of 0.099 to 0.290 m/s (A values o 0.154 to 0.173) are shown in conjunction with the threshold data from Iversen et al. (1987) to recreate their plot of dimensionless threshold parameter (A) as a function of particle friction Reynolds number (Re_{*t}). Threshold data from Burr et al. (2015a) were not included because the definition of threshold in that work is 50% bed motion instead of patches. This plot (Fig. 9) indicates, as concluded by Iversen et al. (1987), that at $Re_{*t} > 10$, A is independent of Re_{*t} within an individual dataset, whereas at Re_{*t} less than 10, the data show significant spread. At the same time, for $Re_{*t} > 10$, A values differ for different experimental conditions. For $Re_{*t} > 10$, A values for data collected in water range from 0.16 (possibly an outlier) to 0.25, whereas for VWT data, they range from 0.13 to 0.20, and for TWT data they range from 0.11 to 0.24. For terrestrial conditions, which have the highest density ratio, the A values for $Re_{*t} > 10$ are the most self-consistent and the lowest, ranging from 0.11 to 0.12. Thus, the A values from the TWT data show the most scatter, approximating the extrema of the other datasets.

3.1. New fit with uncertainties to density ratio function

To investigate our main question as to the effect of density ratio on threshold, these filtered TWT values for A are plotted against density ratio (Fig. 10a). As observed in the plot of particle friction Reynolds number (Re_{*t}), the results show that our data are generally consistent with the previous data, but have greater variability and tend toward higher values of A. We compute new parameters for Eq. (4) including these new TWT data using non-linear least squares fitting. The resulting updated parameters are: $\alpha = 0.214 \pm 0.005$ $\beta = 2.84 \pm 0.24$, $\gamma = 0.014 \pm 0.003$, and $\lambda = 0.68 \pm 0.04$. The uncertainties are derived from a Monte Carlo analysis in which 10,000 trials were run randomly varying the data points within a normal distribution described by their 1-sigma uncertainties. No uncertainties were provided in Iversen et al. (1987) for the data points presented in that paper. Here, we binned those data into groups of low, intermediate, and high-density ratios (ρ_p/ρ less than 12, $12 < \rho_p/\rho$ less than 700, and $\rho_p/\rho > 700$, respectively), based on similarity of experimental conditions under which each dataset was derived, and assigned each data point an uncertainty equal to the standard deviation of the points in its group. A separate analysis using the standard deviation of the seven closest neighbors to each data point produced statistically indistinguishable results. The updated density ratio curve and its corresponding uncertainty envelope are shown in Fig. 10a.

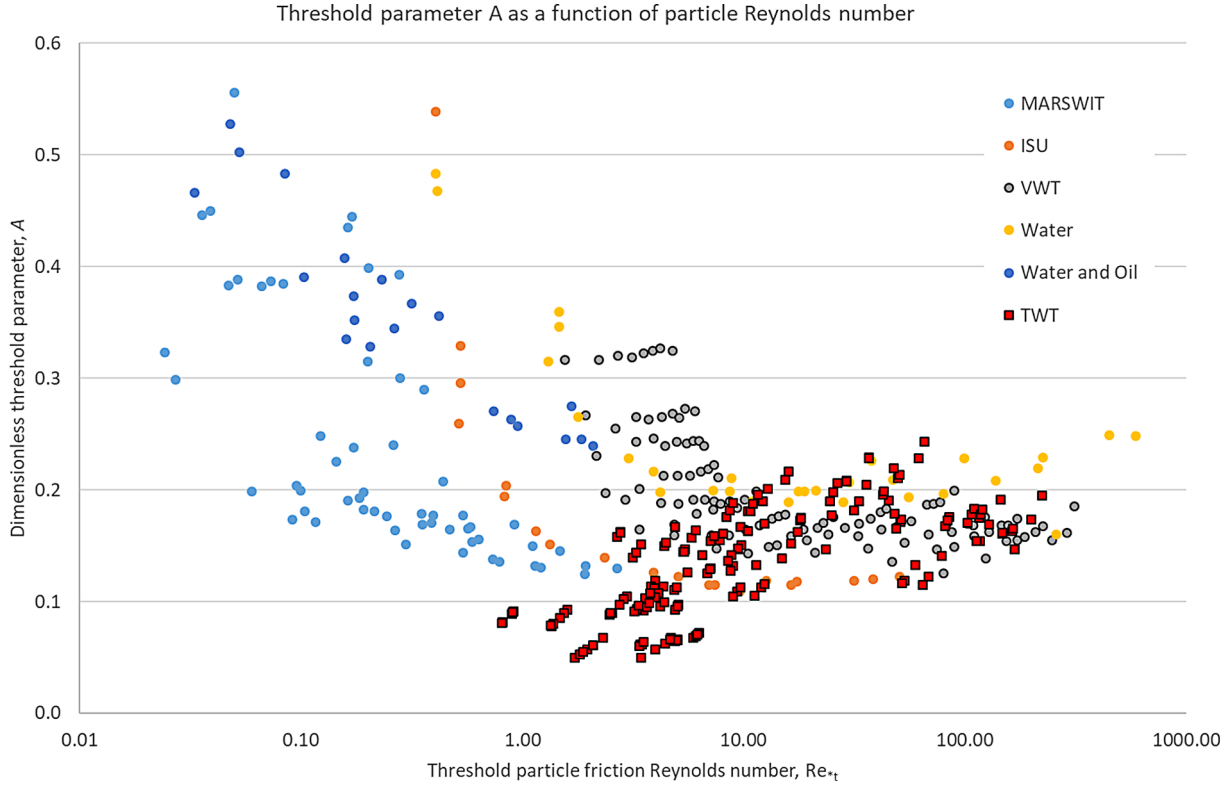

Fig. 9. Threshold parameter A as a function of particle Reynolds number at threshold for a range of fluids and/or pressures. The plot illustrates the independence of friction Reynolds number on A at Re*t> ~10. Above this value, the TWT data are consistent with the VWT data, although they describe a slightly greater range of values for A. The A values for water at Re*t> ~10 tend to plot above the wind tunnel values. See Supplement Materials Fig. 9_for_Supplemental.xlsx for the data used to make this plot, including the TWT data shown in Table 3.

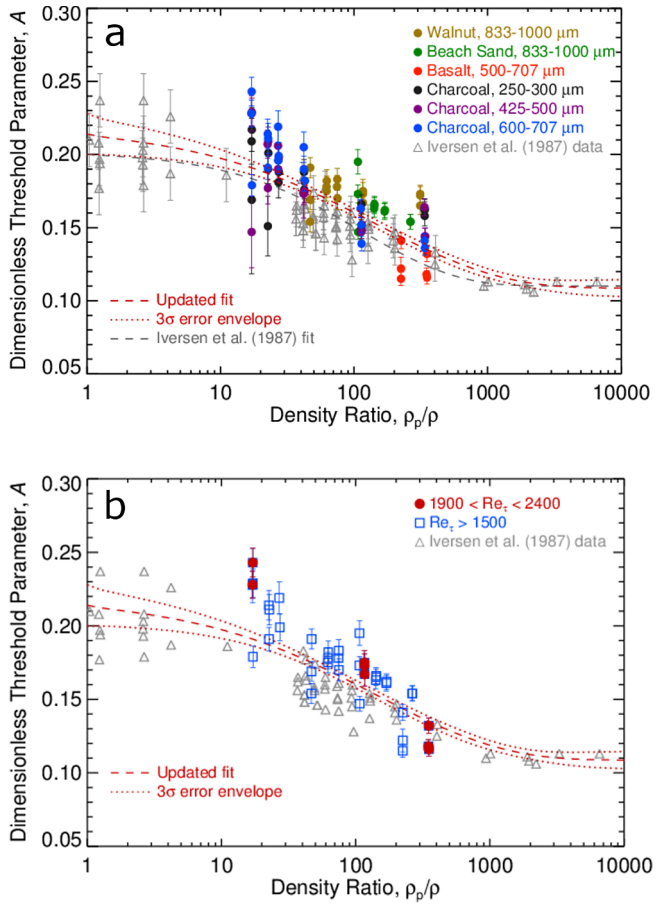

Fig. 10. a) Threshold parameter A, derived from various sources (Iversen et al., 1987), plotted as a function of the density ratio for various fluids for $D_p > 200\,\mu m$ diameter and $Re_{*_t} > 10$. Grey triangles are from Iversen et al. (1987), with uncertainties derived as described in the text. The colored points are the new TWT data presented here. The grey dashed line is the fit from Iversen et al. (1987) with the first exponential parameter corrected as above. The red dashed line is the new fit including the TWT data (data in Table 3) and the Iversen et al. data points. The red dotted lines mark the uncertainty envelope represented by the 3-σ spread in the Monte Carlo fits. See Supplement Materials Fig. 10_for_Supplemental.xlsx for the data used to make this plot. b) TWT data for a limited range of Re_τ to further isolate density ratio dependence, as described in the text. (For interpretation of the references to colour in this figure legend, the reader is referred to the web version of this article.)

4. Discussion

The variability within and among the datasets of A vs Re_{*_t} (Fig. 9) and A vs density ratio (ρ_p/ρ) (Fig. 10) likely has multiple causes, such as the variable shapes (angularity) of the grains within and between experiments and different definitions of threshold between experiments. Of particular interest here and the focus of discussion is the comparison of the two experimental intermediate density ratio datasets that constrain the transitional portion of the curve for the threshold parameter, A.

4.1. Similar negative slopes for the two intermediate density ratio datasets

The two intermediate datasets, from VWT and TWT experiments, exhibit similar negative slopes for A vs density ratio (Fig. 10). This finding confirms the presence and slope of a gradual transition regime, previously derived experimentally from the VWT dataset alone (Iversen et al., 1987), between high dimensionless threshold values for low density ratio conditions and low dimensionless threshold values for high density ratio conditions.

4.2. Sources of the offset between intermediate density ratio data from the VWT and the TWT

Although the two datasets in this transition region show similar negative slopes for A vs density ratio, they also exhibit an apparent offset. This offset could be a consequence of different definitions of threshold both between those two aeolian datasets (Table 2). The definition of threshold for the VWT data as "the speed at which groups of grains began to saltate sporadically" (Greeley et al., 1984) might imply temporally intermittent, as well as spatially limited, saltation. The definition of threshold used for the TWT, namely, "the speed at which continuous grain movement occurred in discrete patches over less than 50% of the bed", likewise implies spatially limited saltation, but contrariwise implies temporally consistent saltation. If correctly interpreted, this threshold criterion using for the VWT experiments of both temporally and spatially intermittent grain motion would be reached at lower wind speeds than the TWT criterion of spatially limited but temporally continuous grain motion. Thus, these two slightly different definitions could yield systematically higher values for the TWT data than for the VWT data as an experimental artifact without a physical difference.

An alternative or additional possible cause for the offset in these intermediate density ratio datasets could be the different values of kinematic viscosity. The use of density as the similitude parameter for the VWT threshold experiments results in a kinematic viscosity of $2.3 \times 10^{-7}\ m^2/s$ (approximately one-half that on the surface of Venus, as noted by Greeley et al. 1984), whereas the use of kinematic viscosity as the similitude parameter for the TWT threshold work resulted in a value of $1.2 \times 10^{-6}\ m^2/s$. This order of magnitude difference in this boundary condition might account for (some portion of) the offset between the VWT and TWT data.

One way that kinematic viscosity could have influenced the results is through its influence on the development of the boundary layer with distance along the test plate. Sufficient test section length is necessary in sedimentary wind tunnel experiments to allow full development of the boundary layer and maturation of the sediment-fluid interactions (e.g., White, 1996; McKenna Neuman et al., 2013). The VWT threshold experiments were performed at a pressure of 30 bar (30×10^5 Pa; Greeley et al., 1984), whereas the TWT experiments were performed at 12 bar (12×10^5 Pa). One measure of a minimum test length, L, needed to achieve a turbulent boundary layer is $L \geq 0.89(\delta^{11}\ g/\nu^2)^{1/8}$, where g is gravity (Iversen, 1991, citing Cermak 1982). For these TWT data collected between 3 and 15 bars (3 and 15×10^5 Pa), with a kinematic viscosity of $1.2 \times 10^6\ m^2/s$ and a boundary layer height of ~2.3 cm (Fig. 6), this minimum length ranges from ~0.14 m to ~0.21 m. Although boundary layer heights are not available in the data available for the VWT work, using the calculated kinematic viscosity for the 30-bar pressure of those experiments and assuming the same height as for the TWT experiments yields similar values. Compared to the ~1 m distance along the wind tunnel test section at the downwind observation port (Burr et al. 2015b), these values would suggest that this minimum wind tunnel length criterion was met for both the VWT and TWT experiments.

At the same time, our experimental data are qualitatively consistent with, though not uniquely diagnostic of, the possibility that the boundary layer for the TWT experiments was not fully developed. In wind tunnel experiments to investigate the effects of a developing boundary layer, values of threshold friction wind speed were found to span an unexpectedly wide range (Williams et al., 1994). Under increasing wind speeds close to threshold, the grains moved in episodic flurries, consistent with entrainment by burst-sweep events, and threshold speeds decreased from the leading edge of the plate downwind. In TWT threshold experiments at 12 bar (12×10^5 Pa; Burr et al., 2015a), observations at the upwind and downwind ports (e.g., run T-12-143) suggested that entrainment was occurring preferentially at the upwind port. The post-experimental appearance of the test plate

showed that volumetrically more entrainment had occurred at the upwind edge, although the shape of the upwind scour marks pointed to vortex shedding as a dominant cause. TWT experiments with sub-sand grain sizes (60 μm; T-12-166 to T-1-168) exhibited episodic motion, consistent with entrainment by burst-sweep events inferred in the developing boundary layer experiments of Williams et al. (1994), though episodic motion might also be a potential effect of enhance interparticle force at small grain sizes. The lack of a fully developed turbulent boundary layer is consistent with a shifting of the TWT data to higher – and more varied – values than derived from the higher-pressure (30 bar or 30×10^5 Pa) VWT work, for which the tunnel was hydrodynamically longer. A longer and/or more fully instrumented test section would provide data to test this interpretation.

4.3. Other possible physical interpretations of the density ratio data

A re-evaluation of the dependencies of A on various physical parameters yields the conclusion, in agreement with Iversen et al. (1987), that dependencies on the particle friction Reynolds number (Re_*) and particle cohesion are primary (Lu et al. 2005). However, these authors suggest a secondary dependence on turbulent velocity variations within the flow, as characterized by the flow Reynolds number ($Re_\tau = u_*\delta/\nu$), in addition to a density ratio effect. Other recent work also points out a possible contribution to entrainment of velocity variations due to flow turbulence (Pähtz et al. 2018). Both of those previous works show that the Re_τ contribution could lead to a dependence on boundary layer height, if the other flow properties and conditions were similar. As illustrated in Fig. 6, δ was ~2.3 cm for all of experiments presented here, so the observed trend of decreasing A with increasing density ratio in these data is not likely due to a dependence on δ alone.

Nevertheless, ν and u_* do vary in these TWT experiments, leading to a range of Re_τ from ~200 to ~6000. Selecting a narrow range of Re_τ (1900 to 2300), shown as red filled circles in Fig. 10b, the scatter at a given density ratio is decreased and the trend between A and density ratio is even more apparent. Lu et al. (2005) state that, when all other parameters (e.g., Re_τ) are held constant, their model does show a dependence of A on density ratio. The scatter that we see in our data in Fig. 10a could, therefore, indicate the dependence on Re_τ that they suggest. It could also explain the single medium density ratio datum in Iversen et al. (1987), ice tea grains measured at 1 bar (1×10^5 Pa), that Pähtz et al. (2019) point out has a lower A than values from the TWT and VWT at similar density ratio (Burr et al., 2015a, Iversen et al. 1987; note that this Iversen et al. datum does not satisfy the $Re_* > 10$ criterion we impose). We include on Fig. 10b all of our new TWT measurements for which $Re_\tau > 1500$ (blue squares). Although they show somewhat more scatter than the more tightly selected red circles, they still illustrate the trend of A with density ratio; the additional scatter could potentially be a consequence of the suggested Re_τ dependence.

Burr et al. (2015) used kinematic viscosity (ν) as the similitude parameter for conducting TWT experiments as analogs for sediment entrainment on Titan. If the second-order flow effects due to turbulent fluctuations proposed by Lu et al. (2005) are important, it is possible that Re_τ may be a better similitude parameter for future analog threshold experiments. Pähtz et al. (2018) suggest experiments in the TWT at ambient (i.e., 1 bar) conditions to test the role of turbulent fluctuations in the flow. At one bar, the fan in the TWT can produce winds sufficient to move only very low-density materials, so 1 bar experiments at high density ratios (>a few hundred) are not currently possible. Improved capabilities and instrumentation of the TWT would both support this suggestion and enable a quantitative understanding of the turbulence occurring during experiments and so provide data for assessing the turbulence similitude to natural conditions.

Initiated by the mismatch between previous TWT data (Burr et al. 2015a) and the density ratio curve based on VWT data (Iversen et al., 1987), this research aimed to investigate the validity of, and physical mechanisms for, the density ratio parameter. The introduction of the density ratio into the expression for A (Eq. (5)) in order to fit the expression to VWT data causes A to tend toward 0.11 at high values of density ratio, recovering the threshold expression from low atmospheric density conditions (as on Earth and Mars). The additional consideration of density ratio was justified on the basis of the reduced effect of impact under higher atmospheric density conditions (Iversen et al., 1987), and this reduced effect of impact has since been reaffirmed in numeric modeling (Kok et al., 2012). Initial analysis of the high-speed video collected as part of this experimental work points to different physical mechanisms for entrainment under different density ratio conditions (Sutton et al., 2018a,b). These low-ejection angle mechanisms include rotational, translations, and skipping motions, instead of the wide range of post-image ejection angles up to near-vertical under ambient Earth conditions (e.g., O'Brien and McKenna Neuman, 2016). We speculate that these unusual entrainment mechanisms result from a difference in the relative importance of the fluid threshold, where grain entrainment is primarily due to fluid flow, and impact threshold, where grains are entrained primarily due to impact by grains in transport. By increasing the effective surface roughness, active saltation increases the effective u_* for a given freestream wind speed (Eq. (7); e.g., Raupach et al., 1993), which adds complication to the accurate identification of threshold. Quantifying the prevalence of these different mechanisms under different density ratio conditions, along with high spatial and temporal resolution data of conditions within the wind tunnel, would provide information to test these preliminary findings, as well as assess the influence of boundary conditions on the quantitative threshold data.

Numerical simulations by Durán et al. (2012) indicate that density ratio is a controlling factor in entrainment and grain transport. Those simulations show a transition between fluid threshold at $\rho_p/\rho \lesssim 10$ and impact threshold at $\rho_p/\rho >$ a few hundred, in agreement with experimental results shown in Fig. 9. Those numerical results might therefore suggest that entrainment in the transition region, where the TWT data lie, involves a combination of fluid and impact processes. Although in qualitative agreement with data, the slope of A vs density ratio in their numerical work does not match the slope of the TWT or VWT data, nor do the numerical results quantitatively agree with A for the fluid or impact endmembers in Fig. 9. This lack of quantitative agreement of their model with other physical measurements was noted by Durán et al. (2012) and attributed to assumption and simplifications (e.g., 2D nature) of their model. Nevertheless, the qualitative agreement is physically instructive and may indicate that the density ratio dependence is a natural transition in entrainment mechanism due to a decreasing influence of impacts with decreasing density ratio.

5. Conclusions

As aeolian processes throughout the Solar System become increasingly apparent (e.g., Lorenz and Zimbelman, 2014 and references therein; Burr et al., 2015b and references therein; Diniega et al., 2017; Jia et al., 2017; Telfer et al., 2018), understanding the controlling physics under this wide range of boundary conditions becomes increasingly important. The results of this investigation into the effect of the density ratio on grain entrainment within the transition region are consistent with the previously derived curve for dimensionless threshold parameter vs density ratio, although more variable and slightly offset to higher values. Thus, we find that the slope of these new data confirms the previous single dataset in this transitional region, while also considering whether the dimensions of the wind tunnel might, at these intermediate fluid densities, introduce unknown artifacts. The updated empirical formulation includes uncertainties for estimating threshold wind speed over a range of density ratios and planetary atmospheric conditions. This work highlights the unique opportunity provided by planetary wind tunnels to explore and understand aeolian processes in our planetary system and likely in others, while at the same time reinforcing the idea that accurate simulation of

planetary boundary conditions is both vital to achieving robust results (e.g., Burr et al. 2015b) and a continued challenge with current facilities. Aeolian *in situ* data from the on-going Mars Science Laboratory and InSIGHT landed missions (Banfield et al., 2020) enable comparison with results from the MARSWIT, as will the future Mars 2020 lander (e.g., Chojnacki et al. 2018), and proposed aeolian missions to Mars would strongly augment these *in situ* data (Newman et al., 2019). Likewise, *in situ* data from the Dragonfly mission (Turtle et al., 2018) will yield values for comparison to these TWT results. More broadly, planetary surface data will provide information for assessing the results of wind tunnel studies, augmenting and strengthening their usefulness as a foundation for understanding extraterrestrial aeolian processes.

6. Data availability

Examples of the videos showing different stages of motion are provided in the Supplemental Online Material, along with a spreadsheet (from which Table 3 is summarized) showing the data collected at both increasing and decreasing wind speeds. Other data, including the raw data collection sheets, experimental data reduction spreadsheets and BLP data reduction spreadsheets (with manufacturer calibration curves) and complete experimental videography cannot be made available due to their size as Supplemental Material on an Elsevier website or on a publicly accessible website such as Mendeley. However, they are freely available from the lead author; please contact them to arrange for transfer of the data associated with this publication.

CRediT authorship contribution statement

Devon M. Burr: Conceptualization, Methodology, Investigation, Resources, Visualization, Supervision, Project administration, Funding acquisition. **Stephen L.F. Sutton:** Methodology, Data curation, Investigation, Writing - review & editing, Visualization. **Joshua P. Emery:** Formal analysis, Investigation, Software, Writing - review & editing, Funding acquisition. **Emily V. Nield:** Data curation, Formal analysis, Investigation. **Jasper F. Kok:** Writing - review & editing. **James K. Smith:** Investigation, Resources. **Nathan T. Bridges:** Investigation.

Declaration of Competing Interest

The authors declare that they have no known competing financial interests or personal relationships that could have appeared to influence the work reported in this paper.

Acknowledgements

The data collection for this work was supported in part by a NASA Planetary Data Analysis, Restoration and Tools (PDART) grant NNX15AJ63G to DMB, JPE, and NTB, which also supplied partial graduate assistantship support for EVN. Additional support was provided by a NASA Outer Planets Research grant **NNX14AR23G** to NTB, DMB, and JFK. We thank Kirby Runyon, Francis Turney, and Xinting Yu for helpful conversations during the data collection and reduction phase of this work and the editors as Aeolian Research for their handling of this manuscript.

Appendix A. Supplementary data

Supplementary data to this article can be found online at https://doi.org/10.1016/j.aeolia.2020.100601.

References

A'Hearn, M.F., Belton, M.J.S., Delamere, W.A., Feaga, L.M., Hampton, D., Kissel, J., Klaasen, K.P., McFadden, L.A., Meech, K.J., Melosh, H.J., Schultz, P.H., Sunshine, J.M., Thomas, P.C., Veverka, J., Wellnitz, D.D., Yeomans, D.K., Besse, S., Bodewits, D., Bowling, T.J., Carcich, B.T., Collins, S.M., Farnham, T.L., Groussin, O., Hermalyn, B., Kelley, M.S., Kelley, M.S., Li, J.-Y., Lindler, D.J., Lisse, C.M., McLaughlin, S.A., Merlin, F., Protopapa, S., Richardson, J.E., Williams, J.L., 2011. EPOXI at Comet Hartley 2. Science 332 (6036), 1396–1400. https://doi.org/10.1126/science.1204054.

Bagnold, R.A., 1941. The Physics of Blown Sand and Desert Dunes. Methuen, London, pp. 265.

Banfield, D., Spiga, A., Newman, C., et al., 2020. The atmosphere of Mars as observed by InSight. Nat. Geosci. 13, 190–198. https://doi.org/10.1038/s41561-020-0534-0.

Bauer, B.O., Houser, C.A., Nickling, W.G., 2004. Analysis of velocity profile measurements from wind-tunnel experiments with saltation. Geomorphology 59 (1), 81–98. https://doi.org/10.1016/j.geomorph.2003.09.008.

Bennett, S.J., Ashmore, P., Neuman, C.M., 2015. Transformative geomorphic research using laboratory experimentation. Geomorphology v. 244, 1–8. https://doi.org/10.1016/j.geomorph.2014.11.002.

Bridges, N.T., Ayoub, F., Avouac, J.P., Leprince, S., Lucas, A., Mattson, S., 2012. Earth-like sand fluxes on Mars. Nature 485 (7398), 339–342 http://www.nature.com/nature/journal/v485/n7398/abs/nature11022.html#supplementary-information.

Bridges, N.T., Greeley, R., Haldemann, A.F.C., Herkenhoff, K.E., Kraft, M., Parker, T.J., Ward, A.W., 1999. Ventifacts at the Pathfinder landing site. J. Geophys. Res. 104, 8595–8616.

Bridges, N.T., Phoreman, J., White, B.R., Greeley, R., Eddlemon, E.E., Wilson, G.R., Meyer, C.J., 2005. Trajectories and energy transfer of saltating particles onto rock surfaces: Application to abrasion and ventifact formation on Earth and Mars. J. Geophys. Res.: Planets 110 (E12), E12004. https://doi.org/10.1029/2004je002388.

Burr, D.M., Bridges, N.T., Marshall, J.R., Smith, J.K., White, B.R., Emery, J.P., 2015a. Higher-than-predicted saltation threshold wind speeds on Titan. Nature 517 (7532), 60–63. https://doi.org/10.1038/nature14088.

Burr, D.M., Bridges, N.T., Smith, J.K., Marshall, J.R., White, B.R., Williams, D.A., 2015b. The Titan Wind Tunnel: A new tool for investigating extraterrestrial aeolian environments. Aeolian Res. 18, 205–214. https://doi.org/10.1016/j.aeolia.2015.07.008.

Cermak, J.E., 1982. Physical modeling of the atmospheric boundary layer (ABL) in long boundary layer wind tunnel (BLWT). Proceeding of the international workshop on wind tunnel modeling criteria and techniques in civil engineering applications. Cambridge University Press, Gaithersburg, Maryland, USA.

Chepil, W.S., 1958. The use of evenly spaced hemispheres to evaluate aerodynamic forces on a soil surface: Eos. Trans. Am. Geophys. Union 39 (3), 397–404.

Chojnacki, M., Banks, M., Urso, A., 2018. Wind-driven erosion and exposure potential at Mars 2020 rover candidate landing sites. J. Geophys. Res. 123, (2). https://doi.org/10.1002/2017JE005460.

Coleman, N.L., 1967, A theoretical and experimental study of drag and lift forces acting on a sphere resting on a hypothetical stream bed: Proc. 12th Congr. IAHR, v. 3, no. 185–192.

Diniega, S., Kreslavsky, M., Radebaugh, J., Silvestro, S., Telfer, M., Tirsch, D., 2017. Our evolving understanding of aeolian bedforms, based on observation of dunes on different worlds. Aeolian Res. 26, 5–27. https://doi.org/10.1016/j.aeolia.2016.10.001.

Durán, O., Andreotti, B., Claudin, P., 2012. Numerical simulation of turbulent sediment transport, from bed load to saltation. Phys. Fluids 24, 103306. https://doi.org/10.1063/1.4757662.

Ewing, R.C., Hayes, A.G., Lucas, A., 2015. Sand dune patterns on Titan controled by long-term climate cycles. Nat. Geosci. 8, 15–19. https://doi.org/10.1038/NGEO2323.

Golombek, M.P., Arvidson, R.E., Bell, I.J.F., Weitz, C.M., Sullivan, R.J., Christensen, P.R., Soderblom, L.A., Squyres, S.W., Grant, J.A., Crumpler, L.S., Greeley, R., 2006. Erosion rates at the Mars Exploration Rover landing sites and long-term climate change on Mars. J. Geophys. Res. E: Planets 111 p. Article Number E12S10.

Graf, W.H., 1971. Hydraulics of Sediment Transport. Water Resources Publications, Highlands Ranch, CO, pp. 513.

Greeley, R., Iversen, J., Leach, R., Marshall, J., White, B., Williams, S., 1984. Windblown sand on Venus: Preliminary results of laboratory simulations. Icarus 57 (1), 112–124. https://doi.org/10.1016/0019-1035(84)90013-7.

Greeley, R., Iversen, J.D., 1985. Wind as a Geological Process: on Earth, Venus and Titan. Cambridge University Press, Cambridge Planetary Science Series, pp. 333.

Greeley, R., Iversen, J.D., Pollack, J.B., Udovich, N., White, B., 1974. Wind tunnel studies of martian aeolian processes. Proc. R. Soc. London. A Math. Phys. Sci. 341 (1626), 331–360. https://doi.org/10.1098/rspa.1974.0191.

Greeley, R., Kraft, M.D., Kuzmin, R.O., Bridges, N.T., 2000. Mars Pathfinder landing site: Evidence for a change in wind regime from lander and orbiter data. J. Geophys. Res.Planets 105 (E1), 1829–1840.

Greeley, R., Leach, R., White, B., Iversen, J., Pollack, J., 1976. Mars - Wind friction speeds for particle movement. Geophys. Res. Lett. 3, 417–420.

Greeley, R., White, B.R., Pollack, J.B., Iversen, J.D., Leach, R.N., 1977. Dust Storms on Mars: Considerations and Simulations. NASA Technical Memorandum, 78423.

Greeley, R., Leach, R., White, B., Iversen, J., Pollack, J., 1980. Threshold windspeeds for sand on Mars: Wind tunnel simulations. Geophys. Res. Lett. 7 (2), 121–124. https://doi.org/10.1029/GL007i002p00121.

Holstein-Rathlou, C., Merrison, J., Iversen, J.J., Jakobsen, A.B., Nicolajsen, R., Nørnberg, P., Rasmussen, K., Merlone, A., Lopardo, G., Hudson, T., Banfield, D., Portyankina, G., 2013. An environmental wind tunnel facility for testing meteorological sensor systems. J. Atmos. Oceanic Technol. 31 (2), 447–457. https://doi.org/10.1175/jtech-d-13-00141.1.

Iversen, J.D., 1991. The aeolian wind tunnel. NASA Technical Report. Document ID: 19910017751, Accession Number: 91N27065, https://ntrs.nasa.gov/search.jsp?R=19910017751.

Iversen, J.D., Greeley, R., Marshall, J.R., Pollack, J.B., 1987. Aeolian saltation threshold:

the effect of density ratio. Sedimentology 34 (4), 699–706. https://doi.org/10.1111/j.1365-3091.1987.tb00795.x.
Iversen, J.D., Greeley, R., Pollack, J.B., 1976a. Windblown dust on Earth, Mars and Venus. J. Atmos. Sci. 33 (12), 2425–2429. https://doi.org/10.1175/1520-0469(1976)033<2425:wdoema>2.0.co;2.
Iversen, J.D., Pollack, J.B., Greeley, R., White, B.R., 1976b. Saltation threshold on Mars: The effect of interparticle force, surface roughness, and low atmospheric density. Icarus v. 29, 381–393.
Iversen, J.D., White, B.R., 1982. Saltation threshold on Earth, Mars and Venus. Sedimentology 29 (1), 111–119. https://doi.org/10.1111/j.1365-3091.1982.tb01713.x.
Jia, P., Andreotti, B., Claudin, P., 2017. Giant ripples on comet 67P/Churyumov–Gerasimenko sculpted by sunset thermal wind. In: Proceedings of the National Academy of Sciences, pp. 201612176. https://doi.org/10.1073/pnas.1612176114.
Knight, J., 2008. The environmental significance of ventifacts: A critical review. Earth Sci. Rev. 86 (1–4), 89–105. https://doi.org/10.1016/j.earscirev.2007.08.003.
Kok, J.F., Parteli, E.J.R., Michaels, T.I., Karam, D.B., 2012. The physics of wind-blown sand and dust. Rep. Prog. Phys. 75 (10), 106901.
Kok, J.F., 2010. An improved parameterization of wind-blown sand flux on Mars that includes the effect of hysteresis. Geophys. Res. Lett. 37 (12), L12202. https://doi.org/10.1029/2010gl043646.
Lorenz, R.D., Zimbelman, J.R., 2014. Dune Worlds: How Windblown Sand Shapes Planetary Landscapes. Springer.
Lu, H., Raupach, M.R., Richards, K.S., 2005. Modeling entrainment of sedimentary particles by wind and water: a generalized approach. J. Geophys. Res. 110, D24114. https://doi.org/10.1029/2005JD006418.
Marshall, J.R., Fogleman, G., Greeley, R., Hixon, R., Tucker, D., 1991. Adhesion and abrasion of surface materials in the Venusian aeolian environment: Journal of Geophysical Research: Solid. Earth 96 (B2), 1931–1947 doi:10.1029/90JB00790.
Marshall, J.R., Greeley, R., 1992. An Experimental-Study of Aeolian Structures on Venus. J. Geophys. Res. Planets 97 (E1), 1007–1016.
McKenna Neuman, C., Sanderson, S., 2008. Humidity control of particle emissions in aeolian systems. J. Geophys. Res.: Earth Surf. 113 (F2). https://doi.org/10.1029/2007JF000780.
McKenna Neuman, C., Ashmore, P., Bennett S.J., 2013. Laboratory andexperimental geomorphology: examples from fluvial and aeolian systems. In: Shroder, J. (Editor in Chief), Orme, A.R., Sack, D. (Eds.), Treatise on Geomorphology. Academic Press, San Diego, CA, vol. 1, The Foundationsof Geomorphology, pp. 325–348.
Merrison, J.P., Holstein-Rathlou, C., Gunnlaugsson, H.P., Nornberg, P., 2009. A Forthcoming European Mars Simulation Wind Tunnel Facility, 40th Lunar and Planetary Science Conference: Houston, Lunar and Planetary Institute, p. Abstract #1544.
Newman, C., et al., 2019. The Next-Generation Planetary Aeolian and Meteorological Investigation (PAMI) mission concept. Am. Geophys. Union, Fall Meeting, San Francisco, CA, Abstract P33D-14.
Nickling, W.G., 1988. The initiation of particle movement by wind. Sedimentology 35 (3), 499–511 doi:10.1111/j.1365-3091.1988.tb01000.x.
Nield, E.V., 2018. A Wind Tunnel Study of the Effect of Density Ratio on Saltation Threshold. University of Tennessee Knoxville, Thesis, pp. 119.
Nikuradse, J., 1933. Stromungsgesetze in rauhen Rohren: Forschg. Arb. Ing. Wes. 361, 22.
O'Brien, P., McKenna Neuman, C., 2016. PTV measurement of the spanwise component of aeolian transport in steady state. Aeolian Res. 20, 126–138. https://doi.org/10.1016/j.aeolia.2015.11.005.
Pähtz, T., Valyrakis, M., Zhao, X.-H., Li, Z.-S., 2018. The Critical Role of the Boundary Layer Thickness for the Initiation of Aeolian Sediment Transport. Geosciences 8 (9), 314.
Porco, C.C., Helfenstein, P., Thomas, P.C., Ingersoll, A.P., Wisdom, J., West, R., Neukum, G., Denk, T., Wagner, R., Roatsch, T., Kieffer, S., Turtle, E., McEwen, A., Johnson, T.V., Rathbun, J., Veverka, J., Wilson, D., Perry, J., Spitale, J., Brahic, A., Burns, J.A., DelGenio, A.D., Dones, L., Murray, C.D., Squyres, S., 2006. Cassini observes the active south pole of Enceladus. Science 311 (5766), 1393–1401. https://doi.org/10.1126/science.1123013.
Rasmussen, K.R., Valance, A., Merrison, J., 2015. Laboratory studies of aeolian sediment transport processes on planetary surfaces. Geomorphology v. 244, 74–94. https://doi.org/10.1016/j.geomorph.2015.03.041.
Raupach, M.R., Gillett, D.A., dn Leys, J.F., 1993. The effect of roughness elements on wind erosion threshold. J. Geophys. Res. Atmos. https://doi.org/10.1029/92JD01922.
Rubin, D.M., Hunter, R.E., 1987. Bedform alignment in directionally varying flows. Science 237 (4812), 276–278. https://doi.org/10.1126/science.237.4812.276.
Sagan, C., Chyba, C., 1990. Triton's streaks as windblown dust. Nature 346 (6284), 546–548.
Sagan, C., Pieri, D., Fox, P., Arvidson, R.E., Guinness, E.A., 1977. Particle motion on Mars inferred from the Viking lander cameras. J. Geophys. Res. 82, 4430–4438.
Sutton, O.G., 1949. Atmospheric Turbulence. Methuen, London.
Sutton, S.L., Nield, E., Burr, D., Emery, J., Kok, J., Turney, F., Runyon, K.D., Smith, J.K., 2018. Aeolian sediment mechanics on Titan: insights from the Titan Wind Tunnel. Division of Planetary Science Annual Meet., Knoxville, TN, abs. 221.10.
Sutton, S. L. F., E. V. Nield, D. M. Burr, J. P. Emery, J. F. Kok, F. A. Turney, K. D. Runyon, and J. K. Smith (2018) Grainscale mechanics in the Titan Wind Tunnel: Observations of fluid dominated entrainment and transport. Intl Conf. Aeolian Res., Bordeaux, France, June 25-29.
Swann, C., Ewing, R.C., 2016. NASA's Planetary Aeolian Laboratory MARtian Surface Wind Tunnel, 47th Lunar. and Planetary Science Conference: Houston, Lunar and Planetary Institute. p. Abstract #2415.
Telfer, M.W., Parteli, E.J.R., Radebaugh, J., Beyer, R.A., Bertrand, T., Forget, F., Nimmo, F., Grundy, W.M., Moore, J.M., Stern, S.A., Spencer, J., Lauer, T.R., Earle, A.M., Binzel, R.P., Weaver, H.A., Olkin, C.B., Young, L.A., Ennico, K., Runyon, K., 2018. Dunes on Pluto. Science 360 (6392), 992–997. https://doi.org/10.1126/science.aao2975.
Turtle, E.P., and 39 co-authors, 2018, Dragonfly: in situ exploration of Titan's organic chemistry and habitability. Lunar Planet. Sci. 49, abs. 1641, https://www.hou.usra.edu/meetings/lpsc2018/pdf/1641.pdf.
Weitz, C.M., Plaut, J.J., Greeley, R., Saunders, R.S., 1994. Dunes and Microdunes on Venus: Why Were So Few Found in the Magellan Data? Icarus 112 (1), 282–295. https://doi.org/10.1006/icar.1994.1181.
White, B.R., 1979. Soil transport by winds on Mars: Journal of Geophysical Research: Solid. Earth 84 (B9), 4643–4651. https://doi.org/10.1029/JB084iB09p04643.
White, B.R., 1981. Venusian saltation. Icarus 46 (2), 226–232. https://doi.org/10.1016/0019-1035(81)90210-4.
White, B.R., 1996. Laboratory simulation of aeolian sand transport and physical modelling of flow around dunes. Ann. Arid Zone 35 (3), 187–213.
White, F.M., 2006. Viscous Fluid Flow. McGraw-Hill, New York.
Williams, D.A., Smith, J.K. NASA's Planetary Aeolian Laboratory: Status and Update, Fifth International Planetary Dunes Workshop: Houston, Lunar and Planetary Institute 2017 p. Abstract #3002.
Williams, J.J., Butterfield, G.R., Clark, D.G., 1994. Aerodynamic entrainment threshold: effects of boundary layer flow conditions. Sedimentology 41 (2), 309–328. https://doi.org/10.1111/j.1365-3091.1994.tb01408.x.
Yu, X., Hörst, S.M., He, C., Bridges, N.T., Burr, D.M., Sebree, J.A., Smith, J.K., 2017. The effect of adsorbed liquid and material density on saltation threshold: Insight from laboratory and wind tunnel experiments. Icarus 297, 97–109. https://doi.org/10.1016/j.icarus.2017.06.034.